nature cancer

Article

https://doi.org/10.1038/s43018-025-01058-2

Cryoablation plus sintilimab and lenvatinib in advanced or metastatic intrahepatic cholangiocarcinoma: a phase 2 trial

Received: 14 April 2025

Accepted: 10 September 2025

Published online: 1 November 2025

Check for updates

Sijia Gu[1,2,3,6], Qiyu Luo[1,2,3,6], Yalei Zhang[1,4], Ling Qian[1,4], Kun Chen[1,4], Fei Liang[5], Yudi Hu[1,2,3], Runye Zhou[1,2,3], Yating Wang[1,2,3], Jingjing Liu[1,2,3], Zhouyu Ning[4], Litao Xu[4], Zhiqiang Meng[4], Ye Li[1,2,3] ✉ & Peng Wang[1,2,3] ✉

Treatment options for advanced or metastatic intrahepatic cholangiocarcinoma (ICC) are limited. In this single-arm, phase 2 trial (CASTLE-01, NCT05010668), 28 participants with advanced or metastatic ICC who have progressed after chemotherapy were treated with cryoablation, followed by anti-PD1 sintilimab (200 mg every 3 weeks) plus lenvatinib (8–12 mg per day) 2 weeks later. The objective response rate assessed by Response Evaluation Criteria in Solid Tumors version 1.1 was 75.0% (95% confidence interval (CI): 59–91%), meeting the prespecified primary endpoint. Secondary endpoints of disease control rate, median progression-free survival and overall survival were respectively 100% (95% CI: 100–100%), 16.8 months (95% CI: 11.5–not reached (NR)) and 25.4 months (95% CI: 13.3–NR). Treatment was well tolerated. Post hoc multiomics analysis of paired pretreatment and on-treatment tumor biopsies suggested that cryoablation increased the tumor immunogenicity and dendritic cell activation, followed by triggering continuous replenishment of intratumoral $CD8^+PD1^{hi}$ effectors from peripheral blood. The addition of lenvatinib transitioned endothelial cells into inflamed venules to boost lymphocyte influx and targeted tumor stroma to promote $CD8^+PD1^{hi}$ effectors penetrating into tumor cell nests. Therefore, cryoablation combined with sintilimab plus lenvatinib represents a promising approach for the treatment of advanced or metastatic ICC. These findings also support the notion that cryoablation may trigger abscopal antitumor immunity in ICC when combined with lenvatinib and PD1 blockade. ClinicalTrials.gov registration: NCT05010668.

The incidence of biliary tract cancer (BTC), especially intrahepatic cholangiocarcinoma (ICC), is increasing around the world[1]. Systemic chemotherapy with GemCis used to be the standard first-line treatment for persons with advanced BTC[2]. Recently, the addition of anti-PD1/PDL1 therapy to GemCis as first-line treatment for advanced BTC improved survival outcomes[3,4].

Until recently, there was a lack of solid evidence supporting second-line treatment options for persons who experienced progression after first-line GemCis[5,6]. Several targeted agents are recommended for persons with actionable molecular alterations; however, few persons with ICC harbor such aberrations, with 13% to 30% carrying *IDH1* variants and ~20% carrying *FGFR2* fusions or rearrangements[7–9]. FOLFOX (folinic acid, fluorouracil and oxaliplatin) is considered a standard second-line therapy according to the results of the ABC-06 study, in which chemotherapy resulted in a median progression-free survival (PFS) of 4.0 months, median overall survival

A full list of affiliations appears at the end of the paper. ✉e-mail: li_ye@fudan.edu.cn; peng_wang@fudan.edu.cn

(OS) of 6.2 months and objective response rate (ORR) of 5% (Supplementary Table 1)[10]. Immune-checkpoint inhibitors (ICIs) used to produce disappointing results in persons with advanced cholangiocarcinoma in the second-line setting (Supplementary Table 1)[11]. Therefore, further investigations are needed to develop novel ICI-based treatment strategies for advanced BTC, including ICC in the second-line setting.

Cryoablation is a minimally invasive percutaneous technique that involves the insertion of a cryoprobe into the target lesion with alternating freeze–thaw cycles, with the ultimate goal of obliterating a spherical lesion and achieving complete tumor ablation[12]. As a locoregional ablative therapy, cryoablation is emerging as an alternative nonsurgical option for persons with early-stage cancers[13–15]. In addition to its ability to locally eradicate tumors, recent studies suggested that cryoablation can be used as an in vivo vaccination tool in combination with immunotherapies to augment systemic antitumor immunity[16–23]. However, much of the clues explaining the antitumor immunity triggered by cryoablation were based on preclinical models rather than human specimens[24–28].

We hypothesized that localized tumor destruction through partial cryoablation in advanced or metastatic ICC may increase the likelihood of systemic response to ICI therapy through a phenomenon recognized as the abscopal effect. We conducted a proof-of-concept, single-arm, phase 2 trial to test this hypothesis.

Results

Participant characteristics

Between August 24, 2021 and May 12, 2023, 36 participants were assessed for eligibility, of whom 28 were enrolled into this phase 2 trial (CASTLE-01, NCT05010668) (Fig. 1a,b). All eligible participants were histologically diagnosed with locally advanced or metastatic ICC and had radiological evidence of progressive disease at enrollment. All enrolled participants had to have at least two distinct lesions, with one intrahepatic lesion amenable to cryoablation and the remaining lesion(s), either intrahepatic or extrahepatic, designated as the target lesion(s) for response assessment (Fig. 1c). Baseline characteristics for the study population are shown in Table 1 and Supplementary Table 2. The average age of the male (61%) and female (39%) population was 62.6 ± 6.8 years. The Eastern Cooperative Oncology Group (ECOG) scores were 0 for 17 participants (61%), 1 for eight participants (29%) and 2 for the remaining three participants (11%). Five participants (18%) had hepatitis B infection and three (11%) had liver cirrhosis (all graded as Child–Pugh class A). A total of 22 participants (79%) had tumor–node–metastasis (TNM) stage IV disease and two (7%) had stage IIIB disease, while four participants (14%) had postoperative recurrence.

Clinical efficacy

All 28 (100%) participants had lesions that were evaluable for response, which excluded cryoablation-treated areas (Fig. 1c). As described in the protocol, the primary endpoint was confirmed ORR; secondary efficacy endpoints included disease control rate (DCR), duration of response (DOR), PFS and OS according to Response Evaluation Criteria in Solid Tumors (RECIST) version 1.1. Efficacy data are listed in Supplementary Table 3. The investigator-assessed ORR was 75% (95% confidence interval (CI): 59–91%), thereby achieving the prespecified primary endpoint. Of these participants, two (7.1%) achieved a confirmed complete response (CR), 19 (67.9%) achieved a confirmed partial response (PR) and seven (25%) achieved stable disease (SD). The DCR was 100% (95% CI: 100–100%). Figure 1 shows the duration of objective responses (Fig. 1d), overall change in disease burden (Fig. 1e) and change in target tumor burden over time (Fig. 1f). Detailed responses in individual participants are shown in Supplementary Table 4. The median time to response (TTR) was 3.6 months (95% CI: 2.6–6.2) and the median DOR was 17.0 months (95% CI: 7.9–not reached (NR)). As of the data cutoff on March 2, 2024, PFS events had occurred in 15 participants (54%), among whom three were still alive. With a median follow-up time of 16.9 months (95% CI: 14.6–NR), the median PFS and OS were 16.8 months (95% CI: 11.5–NR) and 25.4 months (95% CI: 13.3–NR), respectively (Fig. 1g). Typical images of the 28 participants at baseline and best response after treatment are provided in Fig. 1h and Extended Data Fig. 1.

Safety

To evaluate the safety endpoint, treatment-related adverse events (TRAEs) were collected. TRAEs of any grade occurred in all 28 (100%) participants, with the most common events being fatigue (68%), hypertension (65%), hypoalbuminemia (57%) and hypothyroidism (57%) (Supplementary Table 5). Grade (G)3 TRAEs occurred in ten (36%) participants and included hypertension (three, 11%), hyperbilirubinemia (three, 11%) and decreased white blood cell count (two, 7%). Other G3 TRAEs included fatigue, increased alanine aminotransferase, palmar–plantar erythrodysesthesia syndrome (PPES), increased γ-glutamyl transferase and postoperative hemorrhage (each in one participant). Hyperbilirubinemia, a G4 TRAE, occurred in one (4%) participant and led to treatment discontinuation. Most other TRAEs were reversible by a reduction in lenvatinib (lenva), dose interruption or administration of antihypertensive drugs. Immune-mediated AEs (irAEs) are summarized in Supplementary Table 5 and were mostly G1–G2 (G3–G4 irAEs occurred in four (14%) participants). Systemic corticosteroid use for irAEs was reported in three (11%) participants, attributed to G3 fatigue, G3 PPES and G2 PPES (Supplementary Table 5). No treatment-related deaths occurred.

Dynamic landscape of the tumor immune microenvironment during CASTLE therapy

Exploratory post hoc analyses of baseline and on-treatment liver biopsies and peripheral blood mononuclear cells (PBMCs) were performed to capture dynamic changes in cellular composition, functional status and the localization of cell populations during CASTLE therapy. In total, 58 liver tumor biopsies and 51 PBMC samples were collected from 26 participants at three time points: at baseline, 2 weeks after cryoablation and after two cycles of lenva and sintilimab (lenva + sint) (Fig. 2a and Supplementary Table 6). Response to CASTLE therapy did not correlate with the actionable alterations, including *IDH1* mutations, *MET* and *ERBB2* amplifications, tumor mutational burden (TMB) and PDL1 expression, but correlated with PFS (19.37 months for CR and PR versus 9.77 months for SD; $P = 0.0088$) and OS (25.9 months for CR and PR versus 11.5 months for SD; $P = 0.0012$) (Fig. 2b–e). Bulk RNA transcriptomics of liver biopsies ($n = 22$) revealed a distinct pattern of immune cell infiltration at baseline (Fig. 2f). Among these, 11 (50%) participants were clustered on the basis of a 'hot' tumor phenotype characterized

Fig. 1 | Trial design and participant outcomes. a, Overall trial design. qd, once daily; i.v., intravenous injection; p.o, oral administration; q3w, once every 3 weeks. **b**, Trial screening, enrollment, treatment and discontinuation profile. Participants were considered to have completed treatment if they finished 24 months on lenva + sint. **c**, Lesion selection for cryoablation versus response evaluation. **d**, Duration of treatment exposure and efficacy assessments. PD, progressed disease. **e**, Best percentage change in the sum of the longest diameter of the target lesion from baseline (tumor burden). Each bar represents one participant. The ORR and DCR are listed. *CR was confirmed by the reduction of all pathological lymph nodes to a short-axis diameter < 10 mm, which were the only target lesions in this participant. **f**, Changes in investigator-assessed target tumor burden over time. Tumor responses were measured in accordance with RESICT version 1.1 every 6 weeks after the initiation of immunotherapy. Each line represents one participant. **g**, Kaplan–Meier survival curves for PFS and OS. m, median. **h**, Representative images of three participants with significantly prolonged survival (PR for P02; CR for P03 and P09) at baseline and best response. For **d**–**f**, 28 participants were included.

https://doi.org/10.1038/s43018-025-01058-2

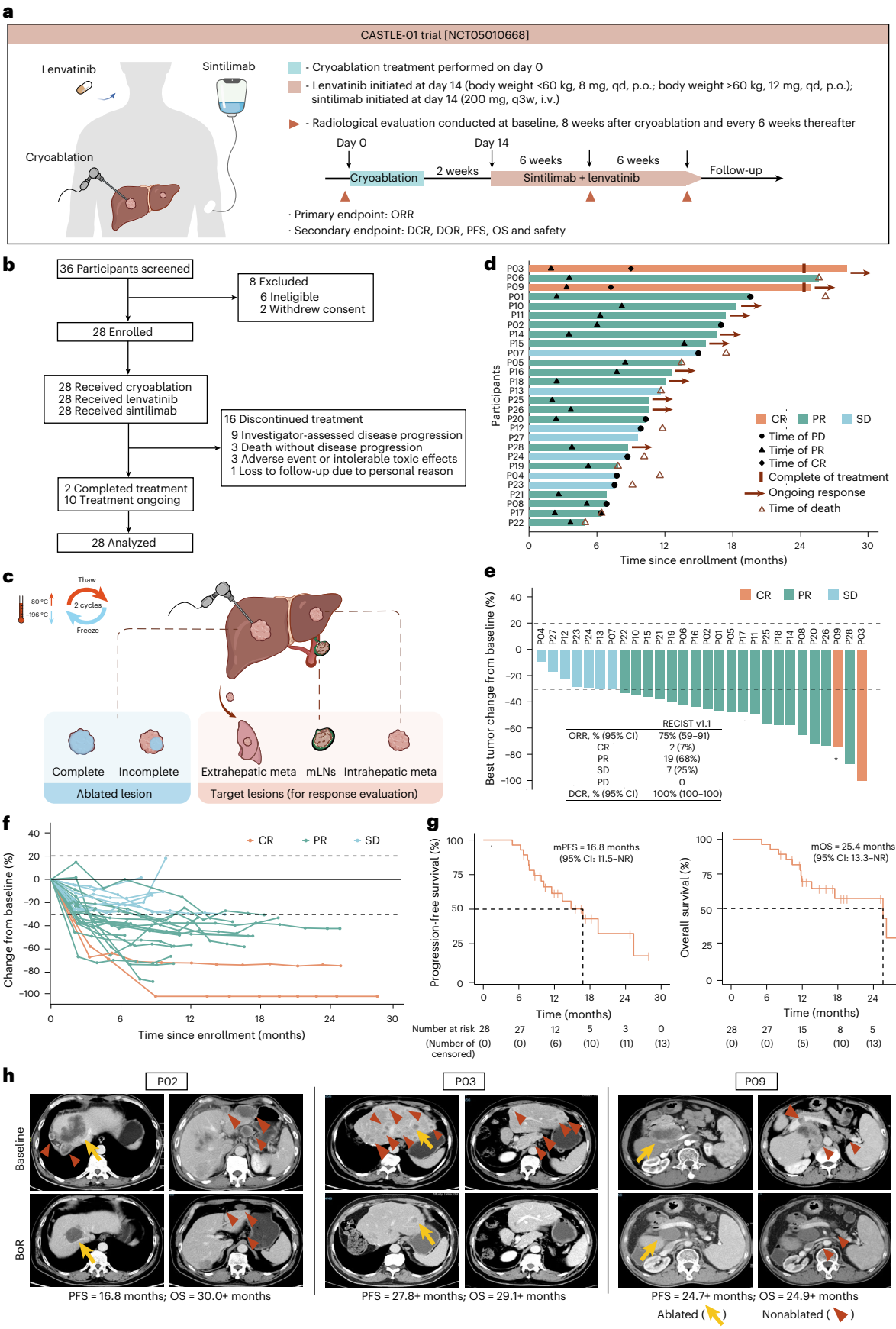

https://doi.org/10.1038/s43018-025-01058-2

Table 1 | Baseline characteristics of participants

All participants (*n*=28)	
Age, years	62.6±6.8
Sex	
Male	17 (60.7%)
Female	11 (39.3%)
ECOG	
0	17 (60.7%)
1	8 (28.6%)
2	3 (10.7%)
Viral hepatitis	5 (17.9%)
Cirrhosis[a]	3 (10.7%)
TNM staging	26 (92.9%)
IIIB	2 (7.1%)
IV	22 (78.6%)
Recurrent	4 (14.3%)
Previous surgery with curative intent	4 (14.3%)
Previous chemotherapy	
GemCis	28 (100%)
Other	3 (10.7%)
Site of metastases	
Lymph node	24 (85.7%)
Lung	4 (14.3%)
Bone	5 (17.9%)
Peritoneum	2 (7.1%)
Other	3 (10.7%)
Maximum tumor size, cm	
<5	5 (17.9%)
≥5	23 (82.1%)
MSI status	
MSS	25 (89.3%)
Not available	3 (10.7%)
PDL1 expression (IHC≥1%)[b]	
Positive	11 (39.3%)
Negative	15 (53.6%)
Not available	2 (7.1%)

MSS, microsatellite stability; IHC, immunohistochemistry. [a]Three participants suffering from liver cirrhosis were all graded as Child–Pugh class A. [b]A tumor proportion score ≥1% was defined as positive.

by increased infiltration of immune cells (especially tumor-infiltrating T cells), upregulation of inhibitory checkpoints, activation of interferon (IFN) responses and increased production of proinflammatory chemokines. The remaining 11 (50%) participants comprised a 'cold' phenotype cluster characterized by scarce or absent T cell infiltration and defects in the IFN pathways. Surprisingly, these tumor phenotypes did not significantly correlate with treatment response. Compared to cold-phenotype participants, those with the hot phenotype did not have a prolonged PFS (16.8 months for hot versus 11.5 months for cold; $P = 0.84$) or OS (25.4 months for hot versus 11.5 months for cold; $P = 0.17$) (Fig. 2g,h). Longitudinal analysis before and after treatment showed that the CASTLE regimen had the potential to turn cold tumors into inflamed, hot tumors (Fig. 2f).

Further single-cell gene expression profiles of 45 paired samples before treatment, after cryoablation and after lenva + sint treatment were obtained to create a single-cell atlas (Fig. 2a and Supplementary Table 6). After filtering low-quality cells and applying batch correction using the R package Harmony, we obtained single-cell RNA (scRNA) profiles from 267,018 cells, identifying immune and nonimmune cell clusters shared across participants and treatments (Extended Data Fig. 2a,b). The major cell types and subclusters were identified using tissue-type-specific canonical marker genes in the scRNA sequencing (scRNA-seq) data (Fig. 2i and Extended Data Fig. 2c,d). Because all participants achieved tumor control (DCR = 100%) and participants with SD achieved a median PFS of 9.77 months, greatly surpassing the historical response to monotherapy or combination therapy with ICIs, we focused on the cellular changes occurring at three treatment time points without comparing the CR + PR and SD groups (Extended Data Fig. 2a,e,f). We also applied imaging mass cytometry (IMC) to gain a spatial-resolution-based phenotyping of the tumor microenvironment (TME) and to validate the scRNA profile results (Fig. 2a). We acquired images from 88 regions of interest (ROIs) derived from 15 paired samples and based on the expression of 30 proteins (Supplementary Table 6), yielding data on 88,924 cells (Extended Data Fig. 2g–i). First, we observed dramatic increases in $CD8^+$ T cells, $CD4^+$ T cells and B cells and a decrease in malignant epithelial cells (EPs) in both scRNA and IMC data (Extended Data Fig. 2a,e,f,j,k). Longitudinal analysis showed that cryoablation induced recruitment of $CD8^+$ effector T cells (Teffs) to the TME, which was boosted by subsequent treatment with lenva + sint (Fig. 2j). Other changes included increased abundance of $CD4^+$ memory T cells following cryoablation. Treatment with lenva + sint significantly decreased the abundances of stalk and tip endothelial cells (ECs), $CD4^+$ T helper (Th)17 cells and regulatory T (Treg) cells, while increasing the abundances of $CD8^+PD1^{hi}$ Teffs, $CD4^+CXCL13^+$ T follicular helper (Tfh) cells, $RELN^+$ cancer-associated fibroblasts (CAFs) and postcapillary venule (PCV) ECs (Fig. 2j). Taken together, our results suggested that the CASTLE regimen reshaped the TME, modulating nonimmunoreactive tumors to become responsive to immunotherapy.

Cryoablation-triggered continuous replenishment of intratumoral $PD1^{hi}$ CD8 Teffs from peripheral blood

We stratified subsets of tumor-infiltrated $CD8^+$ T cells on the basis of expression profiles of pertinent markers (Fig. 3a and Extended Data Fig. 3a). In total, seven discrete $CD8^+$ T cell groups were identified, with four displaying increased PD1 expression (subsets T1–T4) and increased immune response to tumor cells (Fig. 3b and Extended Data Fig. 3b). T1 expressed terminal exhaustion T cell (Tex) markers (*LAG3*, *HAVCR2* and *CTLA4*), T2 displayed increased levels of proliferation markers (*STMN1* and *MKI67*), T3 demonstrated augmented expression of IFN-stimulated gene modules (*MX1* and *ISG15*) and T4 showcased elevated levels of effector molecules (*GZMK* and *EOMES*). The subset of $CD8^+PD1^{hi}$ Teffs in T4 was identified as the precursor population of T1 $CD8^+PD1^{hi}$ Tex, as supported by RNA velocity analysis (Extended Data Fig. 3c–e). Longitudinal analysis showed that cryoablation-induced $CD8^+PD1^{hi}$ Teff recruitment to tumors was boosted after lenva + sint treatment (Fig. 3c and Extended Data Fig. 3f), which was confirmed by IMC data (Fig. 3d,e and Extended Data Fig. 3g,h). Additionally, we observed increased progenitor-like and effector phenotypes and decreased Tex phenotype in $CD8^+PD1^{hi}$ T cells (Fig. 3f,g). Furthermore, the abundance of clonal $CD8^+$ T cells (clone size ≥ 2) in the $CD8^+PD1^{hi}$ Teff cell subset increased after cryoablation and lenva + sint therapy (Extended Data Fig. 3i).

Next, we discovered that cryoablation may promote $CD8^+$ Teff infiltration in two ways by tracing the T cell receptor (TCR) expansion and migration patterns. First, cryoablation induced expansion of preexisting tumor-infiltrating $CD8^+$ Teffs, as evidenced by increased clonal expansion and transition scores of $CD8^+PD1^{hi}$ Teffs (Fig. 3h,i), and increased number and clone size of shared TCRs between baseline and after cryoablation, which was further boosted after treatment

https://doi.org/10.1038/s43018-025-01058-2

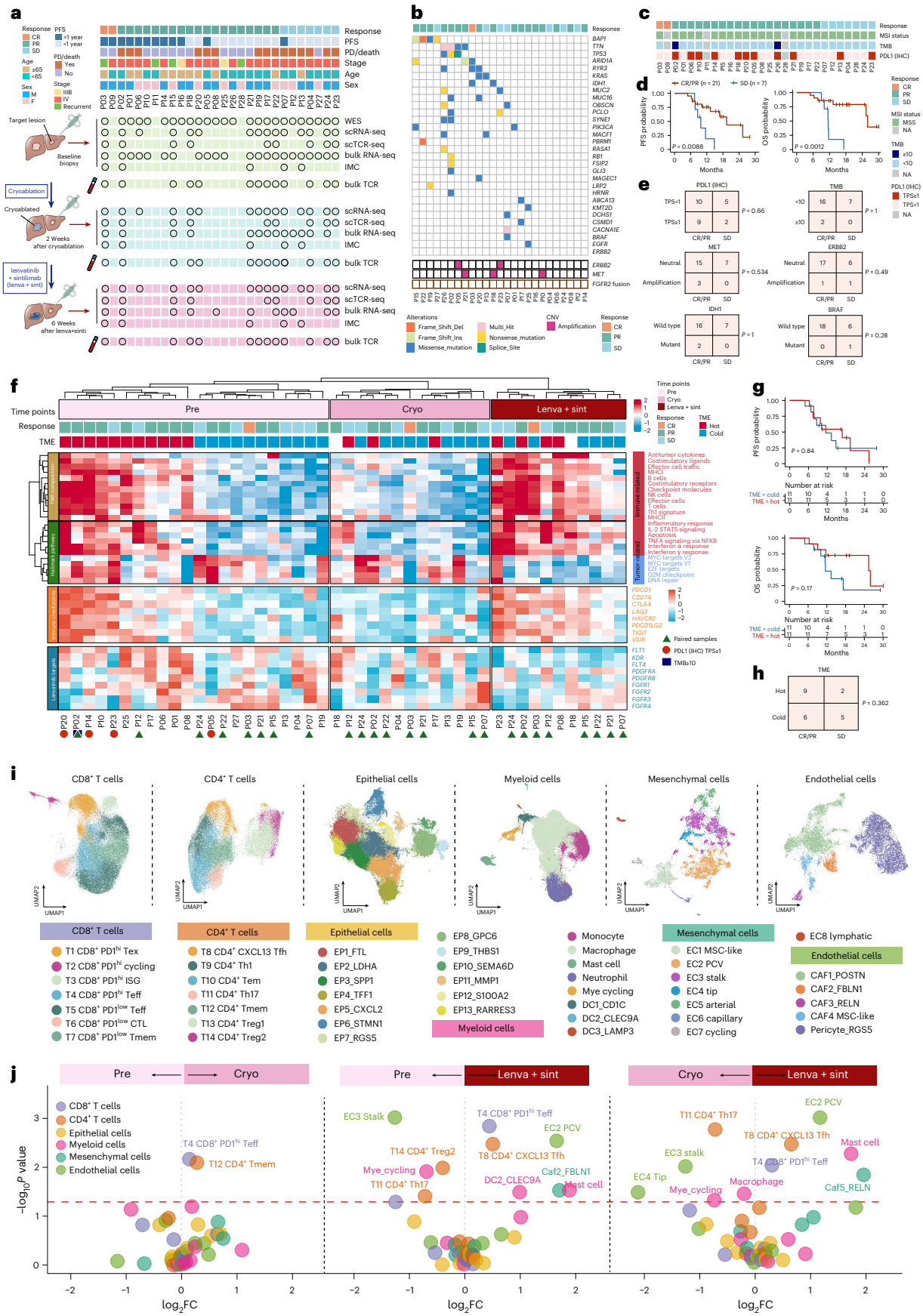

Fig. 2 | Overview of the genomic and transcriptomic landscape of the CASTLE-01 cohort. a, Experimental design of multimodel sequencing, comprising data from tumor tissues and PBMCs collected from the CASTLE-01 cohort of participants with ICC at three time points: before treatment (pre), after cryoablation (cryo) and after lenva + sint (detailed sample collection in Supplementary Table 6). PD, progressed disease. **b**, Mutational landscape in the cohort identified by WES obtained from 25 baseline samples. **c**, MSI status, TMB and PDL1 expression (as determined by IHC) from 28 participants at baseline. **d**, Kaplan–Meier survival curves for PFS and OS in the cohort, analyzed by the log-rank test. **e**, Distribution of treatment responses (CR, PR and SD) by status of biomarkers PDL1 (IHC), TMB, MET, ERBB2, IDH1 and BRAF in pretreatment samples, analyzed by two-sided Fisher's exact test. Participant counts are displayed within the grid. **f**, Heat map of gene set variation analysis scores of representative pathways and expression of selected genes across 46 bulk RNA-seq samples (pre, $n = 22$; cryo, $n = 13$; lenva + sint, $n = 11$) collected from 23 participants at three time points. Hierarchical clustering separated the TME of pretreatment samples into hot and cold phenotypes. Paired, PDL1 (IHC) high-expression and high-TMB samples are labeled. **g**, Kaplan–Meier survival curves of PFS and OS in the cohort, grouped by TME phenotype, analyzed by the log-rank test. **h**, Distribution of treatment responses by TME phenotype in pretreatment samples, analyzed by two-sided Fisher's exact test. Participant counts are displayed within the grid. **i**, UMAP plots of six major cell classes captured across 45 scRNA-seq samples: $CD8^+$ T cells, $CD4^+$ T cells, myeloid cells, EPs, mesenchymal cells and ECs. Colors indicate 48 different cell types. **j**, Proportional changes in cell types across 45 scRNA-seq samples compared pairwise across three treatment time points (each time point, $n = 15$), analyzed by a paired two-sided Wilcoxon test. Colors indicate the cell type assignment. Red dashed lines represent the *P*-value threshold of 0.05. FC, fold change.

with lenva + sint (Fig. 3j,k). Second, we observed a notable emergence of novel clones of tumor-infiltrating $CD8^+$ Teffs after treatment with lenva + sint that were absent at the previous time points (Fig. 3l). These novel clones accounted for 45.6% of cell numbers and 66.8% of the TCR clones of T4 $CD8^+PD1^{hi}$ Teffs in tumors after treatment with lenva + sint (Fig. 3m). They also exhibited smaller clone size and higher expression of progenitor, proliferation and migration markers (Fig. 3n,o) compared to preexisting $CD8^+$ Teffs, suggesting that they recently infiltrated into the TME with a progenitor-like, effector phenotype. Tracking of the emerging novel $CD8^+PD1^{hi}$ Teff clones in the TME after lenva + sint treatment in the peripheral bulk TCR-seq data revealed that, among the 24 TCRs detectable in peripheral blood, 23 (95.8%) emerged in circulation after cryoablation (Fig. 3p,q), indicating that the newly emerged TCRs infiltrated the TME after lenva + sint treatment.

We also identified seven distinct phenotypic clusters of $CD4^+$ T cells in the scRNA-seq data (Extended Data Fig. 3j,k), among which the T8 cluster exhibited high expression of PD1 and CXCL13, characteristic of Tfh cells. T8, defined as $CD4^+CXCL13^+$ Tfh cells, displayed high immune response to tumor cells (Extended Data Fig. 3k) and proportionally increased after lenva + sint therapy (Extended Data Fig. 3l). Positive correlations at a sample level of $CD4^+CXCL13^+$ Tfh cells with $CD8^+PD1^{hi}$ Teffs, B cells and plasma cells were identified (Extended Data Fig. 3m). Examining the immune infiltration based on the hematoxylin and eosin (H&E) stainings also confirmed that both intratumoral and stromal lymphocytes exhibited a significant increase following lenva + sint treatment (Extended Data Fig. 3n–p). Furthermore, after treatment, the formation of tertiary lymphoid structures (TLSs) was observed in P02, who achieved PR (Extended Data Fig. 3q). The signature of TLS was also upregulated after CASTLE treatment in the bulk RNA-seq data (Extended Data Fig. 3r). These findings collectively indicate that the CASTLE regimen had the potential to boost the $CD8^+$ and $CD4^+$ T cells infiltration.

Cryoablation-increased tumor immunogenicity

Cluster analysis of isolated tumor cells revealed a total of 13 distinct EP subgroups (Extended Data Fig. 4a). All subgroups were confirmed to exhibit malignancy using the inferCNV program (Extended Data Fig. 4b). There was upregulation of antigen presentation and the IFNγ and IFNα modules after cryoablation, accompanied by downregulation of the transforming growth factor (TGF)β module after lenva + sint therapy (Fig. 4a and Extended Data Fig. 4c–e). IMC displayed greater abundance of $HLAI^+$ EPs at the two later time points (Fig. 4b,c and Extended Data Fig. 4f). Given the participant specificity of EP9–EP13, we sought to focus on the malignant subgroups EP1–EP8 (Extended Data Fig. 4g). Cryoablation or lenva + sint therapy did not alter the proportions of these subgroups within tumors (Extended Data Fig. 4h). Using the bulk transcriptome data of our cohort, we identified genes related to poor PFS or OS (cutoffs: hazard ratio (HR) > 1 and $P < 0.05$). Interestingly, projection of the two negative gene sets onto the uniform manifold approximation and projection (UMAP) embedding revealed significant enrichment in the EP1 cluster (Fig. 4d,e and Extended Data Fig. 4i,j). Compared to the other malignant EP subgroups, EP1 showed upregulation in glycolysis pathways, alongside downregulation in immune activation-related pathways

Fig. 3 | Cryoablation-triggered continuous replenishment of intratumoral $CD8^+PD1^{hi}$ Teffs from peripheral blood. a, Heat map showing standardized average expression values of cluster-defining genes in $CD8^+$ T cell clusters on population level. **b**, Spearman correlation map showing associations of the proportions of $CD8^+$ T cell subtypes among 15 pretreatment samples in the scRNA-seq data. **c**, Box plot of scRNA-seq data showing the intraparticipant dynamic changes in the frequency of $CD8^+PD1^{hi}$ T cell subtypes in all $CD8^+$ T cells of paired samples stratified by three time points: pre, cryo and lenva + sint (each time point, $n = 12$). **d**, Representative IMC images showing the distribution of $CD8^+PD1^{hi}GZMK^+$ Teffs in participant P02 at the three time points. Scale bars, 100 µm and 50 µm. **e**, Box plot of IMC data showing the dynamic changes in proportion of $CD8^+PD1^{hi}$ Teffs in all $CD8^+$ T cells at the inter-ROI level stratified by the three time points (pre, $n = 32$; cryo, $n = 27$; lenva + sint, $n = 29$; obtained from five participants each time point). **f**, Heat map displaying standardized average expression values in typical genes of T cell-related modules of $CD8^+PD1^{hi}$ T cells at the three time points on population level. **g**, Violin plots showing scores for exhaustion, progenitor, proliferation and effector or memory signatures of $CD8^+PD1^{hi}$ T cells at the three time points. **h**, Intraparticipant clonal expansion levels (left) and clonal transition levels (right) of $CD8^+PD1^{hi}$ Teffs in paired samples at the three time points, quantified using the STARTRAC index. **i**, Alluvial diagram displaying $CD8^+PD1^{hi}$ clonotype-mediated cluster associations. A flow or association among the three time points represents all pairs of cells sharing the same TCR clonotype but may transit to different phenotypes during treatment. **j**,**k**, Violin plot (**j**) revealing the change in clone size of persistent $CD8^+PD1^{hi}$ Teff clones at the three time points at a TCR level (each time point, $n = 40$ clones) and UMAP plot (**k**) displaying the distribution of these clones over time (representing as blue dots). **l**, UMAP distribution of novel clones of $CD8^+PD1^{hi}$ Teffs at the three time points (representing as blue dots). **m**, Pie charts showing the percentage of novel clones of $CD8^+PD1^{hi}$ Teffs among the total preexisting cells (left) and TCR clones (right) at the lenva + sint time point. **n**, Clone size of novel and preexisting clones of $CD8^+PD1^{hi}$ Teffs at the lenva + sint time point at a TCR level. **o**, Dot plots showing the expression levels of selected genes in novel and preexisting clones at the lenva + sint time point. Dot size indicates the percentage of cells in which gene expression was detected; color indicates the mean expression level. **p**,**q**, Frequencies of the TCR nucleotide sequences of novel clones identified in peripheral blood bulk TCR samples at the three time points illustrated by a heat map (**p**) and a box plot (**q**) (each time point, $n = 24$ clones). For **a**,**f**,**g**, data were obtained from 45 scRNA-seq samples at three time points (each time point, $n = 15$). For **h**–**l**, data were obtained from 27 scTCR-seq samples at three time points (each time point, $n = 9$). For **m**–**o**, data were analyzed in nine scTCR-seq samples after lenva + sint treatment. For **c**,**e**,**g**,**h**,**j**,**q**, the center line indicates the median value, bottom and top hinges represent the 25th and 75th percentiles, respectively, and whiskers denote 1.5× the interquartile range. For **c**,**h**,**j**,**q**, a paired two-sided Wilcoxon test was applied. For **e**,**g**,**n**, an unpaired two-sided Wilcoxon test was applied.

https://doi.org/10.1038/s43018-025-01058-2

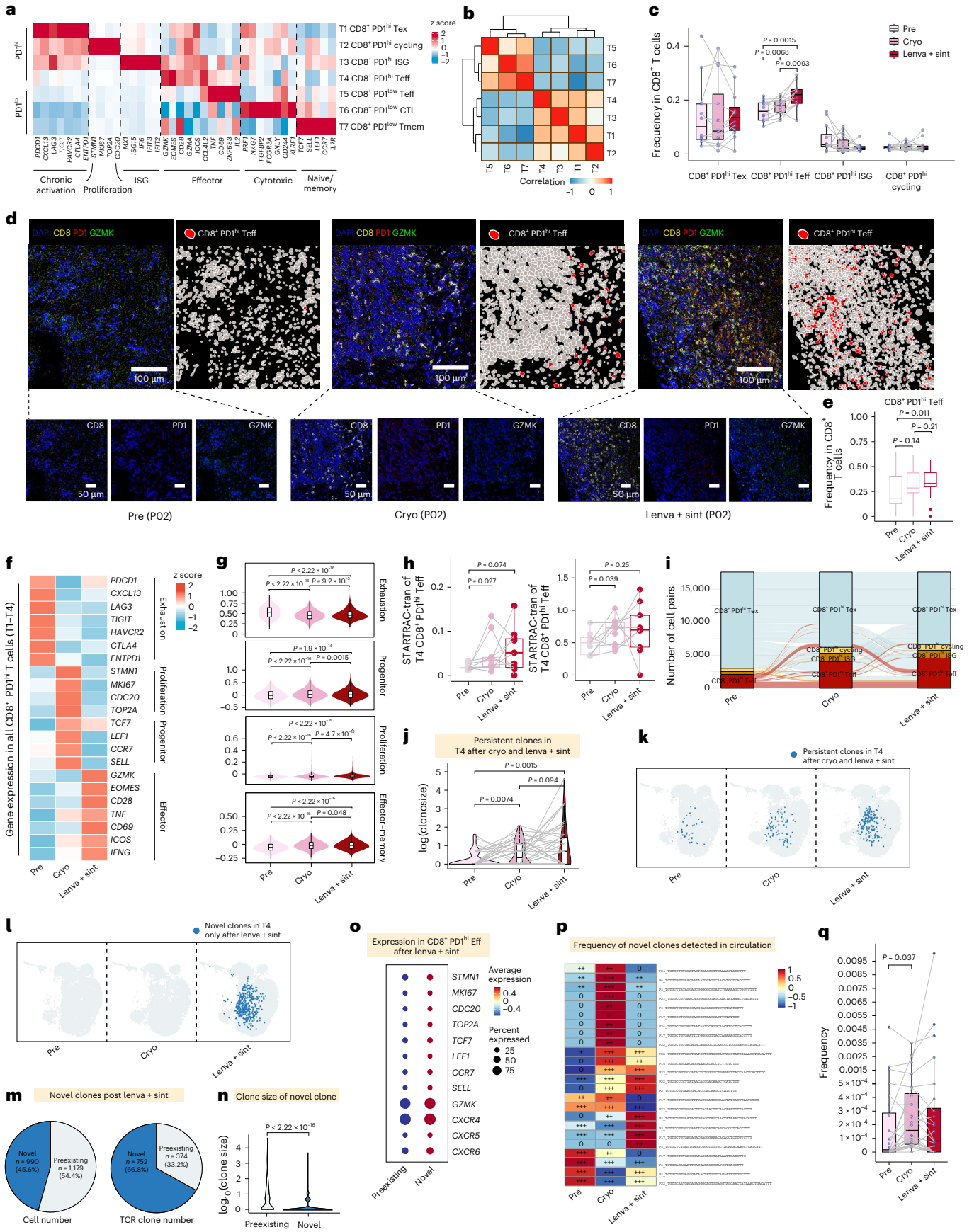

https://doi.org/10.1038/s43018-025-01058-2

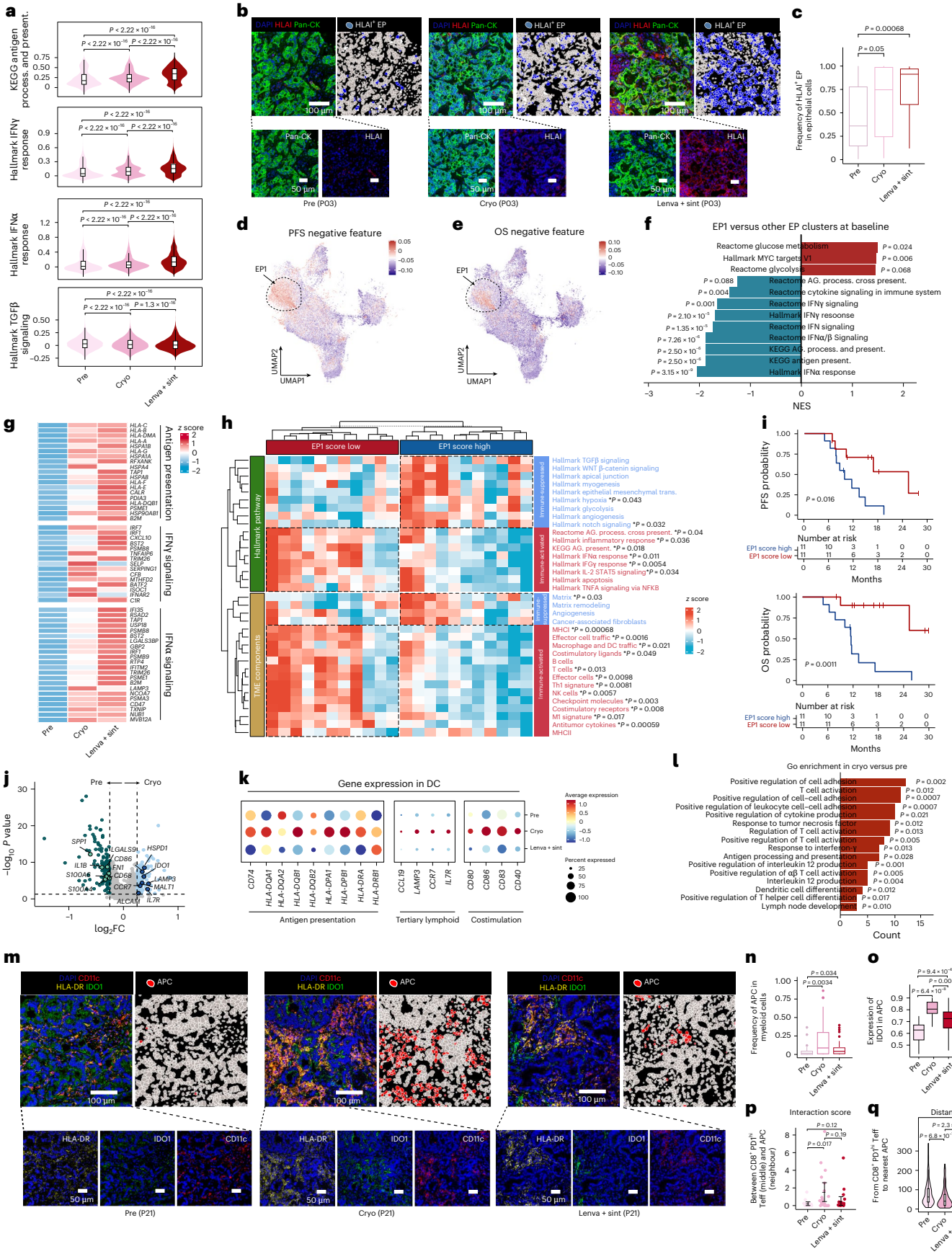

(Fig. 4f). In the context of developmental lineages, EP1 served as the progenitor of other tumor cells (Extended Data Fig. 4k). A notable surge in immune-related gene expression within EP1 subsequent to interventions with cryoablation and lenva + sint therapy was also observed (Fig. 4g and Extended Data Fig. 4l,m). Additionally, immune-related modules including IFNγ, IFNα and antigen presentation were markedly

Fig. 4 | Cryoablation increased tumor immunogenicity and boosted DC activation. a, Violin plots showing the signature scores of Kyoto Encyclopedia of Genes and Genomes (KEGG) antigen processing and presenting, Hallmark IFNγ response, IFNα response and TGFβ signaling in EPs at three time points. **b**, Representative IMC images showing the distribution of HLAI$^+$ EPs of participant P03 at the three time points. Scale bars, 100 μm and 50 μm. **c**, Box plot of IMC data showing the dynamic changes in proportion of HLA$^+$EPs in all EPs at the inter-ROI level stratified by the three time points from five participants. **d**,**e**, UMAP plots of EP clusters colored by gene signatures identified in bulk RNA data related to poor PFS (**d**) and poor OS (**e**). **f**, Comparative gene set enrichment analysis of pretreatment gene sets in the EP1 cluster and other malignant EP clusters in 15 pretreatment scRNA-seq samples. NES, normalized enrichment score. *P* values were determined using a one-tailed permutation test. **g**, Heat map displaying standardized average expression values in typical genes of immune-related modules in EP1 cells at the three time points on population level. **h**, Heat map showing abundance of pathways and TME components per sample in pretreatment bulk RNA-seq samples stratified by median EP1 signature scores into high-EP1 and low-EP1 signature groups. Significantly differentially expressed pathways are indicated (unpaired two-sided *t*-test, $^*P < 0.05$). **i**, Kaplan–Meier survival curves for PFS (left) and OS (right), grouped by EP1 signature scores of pretreatment bulk RNA-seq samples, analyzed by the log-rank test. **j**, Volcano plots showing the genes with differential expression between the time points before treatment and after cryoablation in all DCs in the scRNA-seq data (each time point $n = 15$). The *x* axis and *y* axis values were calculated by the Seurat method. Blue and green dots indicate genes with significant upregulation at the time points after cryoablation and before treatment, respectively. Significant genes of interest are labeled. **k**, Dot plots showing the expression levels of selected genes in all DCs at three time points. Dot size indicates the percentage of cells in which the gene was detected. Color indicates the mean expression. **l**, Numbers of enriched genes (count) of enriched pathways in all DCs at the time points before treatment and after cryoablation (each time point, $n = 15$) in the scRNA-seq data, analyzed by the hypergeometric test. **m**, Representative IMC images showing the distribution of CD11c$^+$HLA-DR$^+$IDO1$^+$ APCs of participant P21 at the three time points. Scale bars, 100 μm and 50 μm. **n**, Quantification of the percentages of APCs in myeloid cells in IMC data at the inter-ROI level stratified by the three time points. **o**, Box plot of IMC data showing the dynamic changes in IDO1 expression in APCs at the inter-ROI level, stratified by the three time points (pre, $n = 17$; cryo, $n = 20$; lenva + sint, $n = 23$; obtained from five participants each time point); ROIs without IDO1$^+$ APCs were excluded from analysis. **p**, Interaction score between CD8$^+$PD1$^+$ Teffs (middle) and APCs (neighbor) in IMC at the inter-ROI level, stratified by the three time points. Black bars indicate the mean and 95% CI. **q**, Quantification of the distance of CD8$^+$PD1$^+$ Teffs to the nearest APC in IMC, stratified by the three time points. For **a**,**d**,**e**,**g**,**k**, data were obtained from 45 scRNA-seq samples at three time points (each time point, $n = 15$). For **a**,**c**,**j**,**n**–**q**, an unpaired two-sided Wilcoxon test was applied. For **c**,**n**,**p**,**q**, ROIs obtained from five participants each time point (pre, $n = 32$; cryo, $n = 27$; lenva + sint, $n = 29$) were analyzed. For **a**,**c**,**n**,**o**,**q**, the center line indicates the median value, bottom and top hinges represent the 25th and 75th percentiles, respectively, and whiskers denote 1.5× the interquartile range.

upregulated in the EP1 subcluster (Extended Data Fig. 4n,o). Using the top differentially expressed genes in the EP1 subgroup, EP1 scores of pretreatment bulk transcriptomic samples were calculated (Supplementary Table 7). Notably, bulk RNA samples with higher EP1 scores exhibited elevated expression of immune inhibitory signaling pathways and greater infiltration of immune inhibitory cellular components (Fig. 4h and Extended Data Fig. 4p,q). Conversely, bulk RNA samples with lower EP1 scores demonstrated abundant expression of immune-activated pathways and TME components. Additionally, immune responses after cryoablation also differed between EP1^{low} and EP1^{high} groups (Extended Data Fig. 4r). At the single-cell transcriptomic level, a significant negative correlation was observed between the proportions of EP1 and CD4$^+$CXCL13$^+$ Tfh and CD8$^+$PD1^{hi} Teff cells (Extended Data Fig. 4s,t). Thus, the baseline EP1 score demonstrated robust predictive value for PFS and OS after CASTLE treatment (Fig. 4i).

Cryoablation-boosted dendritic cell activation and antigen presentation

Dendritic cells (DCs) were categorized into three distinct subgroups: DC1 (*CD1C*), DC2 (*CLEC9A*) and DC3 (*LAMP3*) (Extended Data Fig. 5a,b). The lack of change in the proportions of the DC group and subgroups after cryoablation (Extended Data Fig. 5c,d), likely because of limited DC capture numbers, prompted us to explore functional differences in the subgroups. Representing traditional antigen-presenting cells (APCs), DC1 and DC2 exhibited high expression levels of *CD74* and major histocompatibility complex class II (MHC II) genes (Extended Data Fig. 5e) and enrichment of antigen presentation pathways (Extended Data Fig. 5f). By contrast, DC3 exhibited elevated expression of costimulatory and tertiary lymphoid markers (*CD80*, *CD86*, *CD40*, *CCL19* and *CCR7*) (Extended Data Fig. 5e) and involvement in T cell immunoregulation and migration (Extended Data Fig. 5f).

Fig. 5 | Boosting intratumoral lymphocyte influx through targeting of the tumor vasculature. a, Heat map showing standardized average expression values of cluster-defining genes in eight EC clusters on population level. **b**, Box plot showing dynamic proportional changes in all EC subtypes in paired samples at three time points of scRNA-seq data (each time point, $n = 11$). Data were analyzed using a paired two-sided Wilcoxon test. **c**, Pseudotime-ordered analysis of EC clusters EC1–EC4 in scRNA-seq data. Dot colors indicate pseudotime inferred by Monocle2 (top), cell type (middle) and time point (bottom). **d**, Heat map of the dynamic changes in gene expression along the pseudotime of the EC1–EC4 transition (divided into three phases), showing the distribution of the four EC subtypes over pseudotime. Top: subclusters are labeled by color. Genes showing differential expression during pseudotime (left) and enriched pathways (right) are labeled. **e**, Heat map showing scaled mean activities of selected modules in the eight EC clusters on population level. GO, Gene Ontology. **f**–**i**, Dynamic changes in transcriptional characteristics in EC subclusters at the three time points. Heat maps showing scaled average activities of selected modules in stalk and tip cells (**f**) and PCV cells (**h**) on population level. Dot plots showing the expression levels of selected genes in stalk and tip cells (**g**) and PCV cells (**i**). Dot size indicates the percentage of cells in which the gene was detected. Color indicates the mean expression. **j**, Scatter plots showing significant correlations between the proportion of CD8$^+$PD1^{hi} Teffs in CD8$^+$ T cells and the percentages of stalk cells (top), tip cells (middle) and PCV cells (bottom) in all ECs. Data analyzed by the two-sided Pearson correlation test (top) or the two-sided Spearman correlation test (middle and bottom). **k**, Scatter plots showing significant correlations between the proportion of CD8$^+$PD1^{hi} Teffs in CD8$^+$ T cells of scRNA-seq data and the TVNS in bulk RNA-seq samples (pre, $n = 12$; cryo, $n = 9$; lenva + sint, $n = 9$). Data were analyzed using a two-sided Pearson correlation test. **l**, Kaplan–Meier survival curves for PFS and OS, grouped by high and low TVNSs of 11 bulk RNA-seq samples from the CASTLE-01 discovery cohort after lenva + sint treatment, analyzed using the log-rank test. **m**, Box plot of IMC data showing the dynamic proportional changes in PCV ECs and stalk and tip cells of all ECs at the inter-ROI level, stratified by the three time points. **n**, Representative IMC images showing the distributions of CD31$^+$SELP$^+$HLA-DR$^+$ PCV ECs and CD31$^+$VEGFR2$^+$ stalk and tip cells of participant P03 at the three time points. Red arrows indicate the distribution of CD8$^+$PD1^{hi}Teff. Scale bars, 100 μm and 50 μm. **o**, Box plot of IMC data showing the dynamic changes in HLA-DR expression in PCV ECs and stalk and tip cells at the inter-ROI level stratified by the three time points (PCV HLA-DR expression calculation: pre, $n = 26$; cryo, $n = 19$; lenva + sint, $n = 28$; stalk and tip HLA-DR expression calculation: pre, $n = 31$; cryo, $n = 24$; lenva + sint, $n = 28$). ROIs without PCV ECs or stalk and tip cells were excluded for analysis. **p**, Interaction scores of CD8$^+$PD1^{hi} Teffs with PCV cells (neighbor; left) and stalk and tip cells (neighbor; right) in IMC data at the inter-ROI level, stratified by the three time points. Black bars indicate the mean values and 95% CI. For **a**,**c**–**j**, data were obtained from 45 scRNA-seq samples at three time points (each time point, $n = 15$). For **j**,**k**, the shaded area indicates the 95% CI of the fit. For **m**,**p**, ROIs obtained from five participants each time point (pre, $n = 32$; cryo, $n = 27$; lenva + sint, $n = 29$) were analyzed. For **b**,**m**,**o**, the center line indicates the median value, bottom and top hinges represent the 25th and 75th percentiles, respectively, and whiskers denote 1.5× the interquartile range. For **m**,**o**,**p**, an unpaired two-sided Wilcoxon test was applied.

https://doi.org/10.1038/s43018-025-01058-2

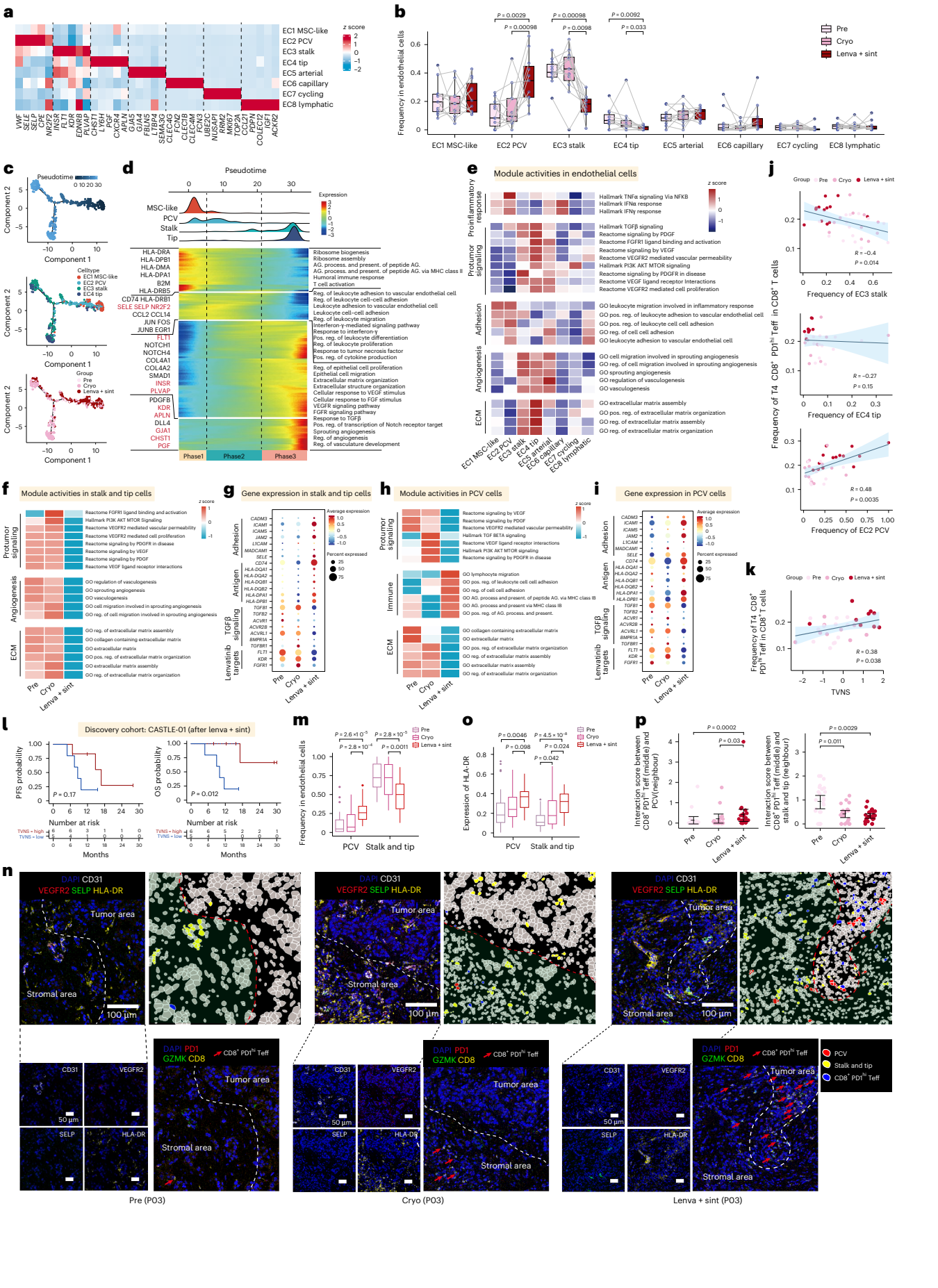

DCs showed upregulation in the expression of antigen presentation and costimulatory genes after cryoablation (Fig. 4j,k), as well as enrichment in immune processes related to T cell activation and DC differentiation (Fig. 4l and Extended Data Fig. 5g,h). After cryoablation, DC1 and DC2 showed further upregulation of the antigen-presentation-related molecules (Extended Data Fig. 5i,j), while DC3 showed enhanced expression of the costimulatory molecules (Extended Data Fig. 5k). In terms of their interaction with T cells, all three subsets of DCs exhibited an upregulated ability to present antigen to T4 $CD8^+PD1^{hi}$ Teffs (Extended Data Fig. 5l). Within the receptor–ligand network, molecules facilitating T cell migration and maturation were also elevated, thus fostering an environment conducive to subsequent immunotherapy (Extended Data Fig. 5o). Consistently, IMC showed a significant increase in the frequency of $CD11c^+HLA\text{-}DR^+IDO1^+$ APCs after cryoablation (Fig. 4m,n, and Extended Data Fig. 5m,n), along with upregulated expression of IDO1 (Fig. 4o), indicative of the IFN response[29]. Furthermore, spatial interaction between APCs and $CD8^+PD1^{hi}$ Teffs was stronger after cryoablation, as evidenced by higher interaction scores and closer distance at spatial resolution (Fig. 4p,q).

While neutrophils may potentially form neutrophil extracellular traps (NETs) after ablation to create an immunosuppressive TME[30], our comprehensive analysis of neutrophil changes following cryoablation revealed a significant reduction in neutrophil proportions along with downregulation of neutrophil activation and chemotaxis-related pathways (Extended Data Fig. 5c,p,q). Multiplex immunofluorescence further confirmed decreased NET formation (Extended Data Fig. 5r,s). Importantly, we observed concurrent upregulation of antigen presentation genes and immune-activating pathways in the scRNA-seq data (Extended Data Fig. 5p,q).

Intratumoral lymphocyte influx boosted by targeting tumor vasculature

In the aforementioned experiments, we noticed that many novel $CD8^+PD1^{hi}$ Teff clones entered circulation after cryoablation. However, these clones only infiltrated tumors after lenva + sint therapy. We speculated that lenva may normalize the tumor vasculature, thus boosting intratumoral lymphocyte influx[31,32]. Therefore, we annotated EC subtypes with markers identified from published datasets, resulting in eight EC clusters[33,34] (Fig. 5a and Extended Data Fig. 6a). Traditional angiogenic cell phenotypes, such as tip cells and stalk cells, were significantly reduced following lenva treatment, possibly because of their elevated expression of vascular endothelial growth factor receptor (VEGFR; *KDR* and *FLT1*)[33] (Fig. 5b). Concurrently, a noticeable increase in PCV ECs, also known as high endothelial venules, which expressed high levels of adhesion markers (*SELE* and *SELP*), were observed after lenva[34] (Fig. 5b). Pseudotime analysis unveiled sequential transcriptional alterations during EC development, with tip and stalk cells at the terminus of the trajectory, indicative of their status in immature neovascularization (Fig. 5c,d and Extended Data Fig. 6b). Pathway analysis indicated that PCV ECs exhibited enrichment in modules associated with proinflammatory effects and lymphocyte adhesion, whereas tip and stalk cells showed enrichment in pathways related to tumor promotion, angiogenesis and extracellular matrix (ECM) regulation (Fig. 5d,e and Extended Data Fig. 6c). The use of lenva upregulated genes related to cytokine ligands, cell adhesion and antigen presentation, while downregulating TGFβ-related genes and lenva-targeting genes (Extended Data Fig. 6d). These observations were verified in pathway analysis (Extended Data Fig. 6e). Specifically, lenva decreased the expression of angiogenesis and ECM modules in stalk and tip cells (Fig. 5f,g and Extended Data Fig. 6f) while increasing immune-related functions, including antigen presentation and cell adhesion, in PCV cells (Fig. 5h,i and Extended Data Fig. 6g). Furthermore, the frequency of $CD8^+PD1^{hi}$ Teff and $CD4^+CXCL13^+$ Tfh cells was positively correlated with PCV ECs but negatively correlated with stalk and tip cells (Fig. 5j and Extended Data Fig. 6h), suggesting an association between vasculature normalization and lymphocyte influx.

Therefore, to better characterize the effects of lenva, we calculated a tumor vascular normalization score (TVNS) in the bulk RNA-seq data as follows: $(\text{PCV score}/(\text{stalk score} + \text{tip score}))_{z\ \text{score}}$ (Extended Data Fig. 6i and Supplementary Table 7). TVNSs were positively associated with the frequency of tumor-infiltrated $CD8^+PD1^{hi}$ Teffs (Fig. 5k). Notably, TVNSs following lenva therapy but not at baseline or after cryoablation predicted the PFS and OS of CASTLE-01 participants (Fig. 5l and Extended Data Fig. 6j). The value of TVNSs for predicting immunotherapy response could be verified in participants with advanced hepatocellular carcinoma who received atezolizumab plus bevacizumab, an anti-VEGF antibody, in the IMbrave150 and GO30140 trials[29,30] (Extended Data Fig. 6k).

Next, we examined the dynamic changes in these three types of lenva-associated ECs in the spatial dimension (Extended Data Fig. 6l). Consistently, IMC revealed an increased proportion of PCV ECs and decreased proportions of stalk and tip cells following lenva treatment

Fig. 6 | Targeting of CAFs involved in the response to CASTLE therapy. a, Heat map showing standardized average expression values of cluster-defining genes in mesenchymal cell clusters on population level. **b**, Heat map showing scaled mean activities of selected module in CAF subgroups on population level. **c**, Box plot of scRNA-seq data showing dynamic proportional changes in mesenchymal cell subtypes of paired samples stratified by three time points, analyzed by the two-sided paired Wilcoxon test. **d**,**e**, Dynamic changes in transcriptional characteristics of CAF1 cells at three time points, as illustrated by a heat map showing scaled average activities of selected modules on population level (**d**) and a dot plot showing the expression levels of selected genes (**e**). Dot size indicates the percentage of cells in which the gene was detected. Color indicates the mean expression. **f**, Scatter plots showing significant correlations of the percentage of CAF1 among mesenchymal cells with the proportion of $CD8^+PD1^{hi}$ Tex cells among $CD8^+$ T cells (left) and the exhaustion score in $CD8^+PD1^{hi}$ T cells (right). Data were analyzed using a two-sided Spearman correlation test (left) or two-sided Pearson correlation test (right); the shaded area indicates the 95% CI of the fit. **g**, Heat maps showing NicheNet analysis in the scRNA-seq data of the regulatory potential of inferred prioritized ligands in CAF1 to the predicted target genes in $CD8^+PD1^{hi}$ T cells and the inferred prior interaction potential of these ligands to receptor genes in $CD8^+PD1^{hi}$ T cells (middle), scaled mean expression of ligands in CAF1 (left) and scaled mean expression of selected genes in $CD8^+PD1^{hi}$ T cells (bottom) at the three time points. **h**,**i**, Dynamic changes in transcriptional characteristics of CAF3 cells at the three time points on a population level, as illustrated by a heat map showing scaled average activities of selected modules (**h**) and a dot plot showing the expression levels of selected genes (**i**). Dot size represents the percentage of cells in which the gene was detected. Color indicates the mean expression. **j**, Receptor–ligand pairs with significant differences inferred using scRNA-seq data between the three time points, based on CAF3 with $CD8^+PD1^{hi}$ Tex cells and $CD8^+PD1^{hi}$ Teffs. The larger dot size indicates a significant *P* value. Colors illustrate the communication probability. **k**, Representative IMC images showing the distribution of FAP^+SMA^+collagen$^+$ myCAFs, FAP^+FBLN5^+ iCAFs and $FAP^+FBLN5^+HLA^+$ apCAFs of participant P02 at the three time points. Red arrows indicate the distribution of $CD8^+PD1^{hi}$Teff. Scale bars, 100 μm and 50 μm. **l**, Box plot of IMC data showing the dynamic proportional changes in myCAFs, iCAFs and apCAFs in mesenchymal cells at the inter-ROI level, stratified by the three time points. **m**, Violin plots of the distance between $CD8^+PD1^{hi}$ Teffs and the nearest myCAF (left) and EPs and the nearest $CD8^+PD1^{hi}$ Teff (right) at the three time points. **n**, Interaction scores of $CD8^+PD1^{hi}$ Teffs with myCAFs (neighbor; left) and EPs with $CD8^+PD1^{hi}$ Teffs (neighbor; right) in IMC at the inter-ROI level, stratified by the three time points. Black bars indicate the mean values and 95% CI. For **a**–**j**, data were obtained from 45 scRNA-seq samples at three time points (each time point, $n = 15$). For **c**,**l**,**m**, the center line indicates the median value, bottom and top hinges represent the 25th and 75th percentiles, respectively, and whiskers denote 1.5× the interquartile range. For **l**–**n**, ROIs obtained from five participants each time point (pre, $n = 32$; cryo, $n = 27$; lenva + sint, $n = 29$) were analyzed and an unpaired two-sided Wilcoxon test was applied.

https://doi.org/10.1038/s43018-025-01058-2

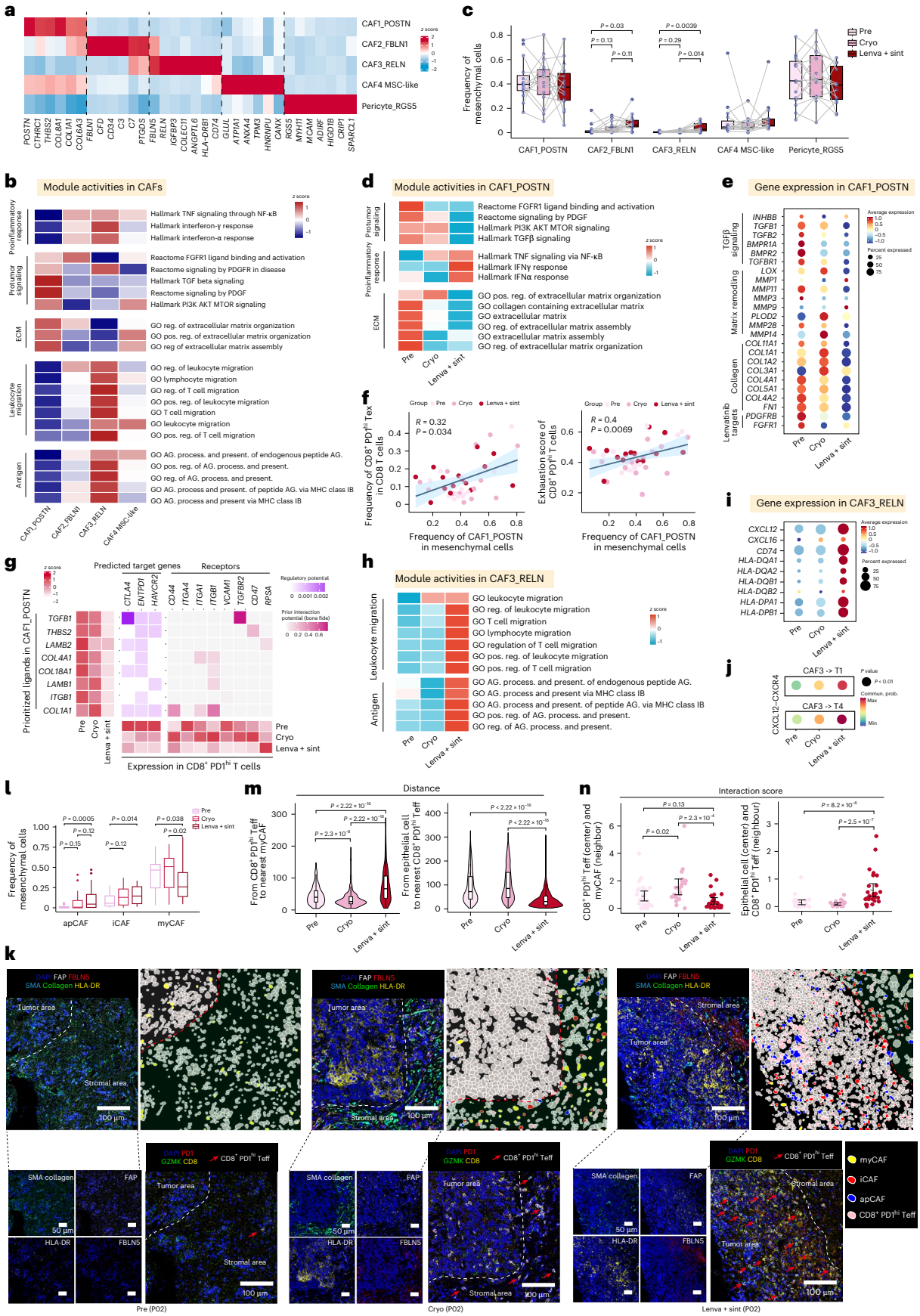

(Fig. 5m,n and Extended Data Figs. 4n and 6m,n), accompanied by enhanced expression of HLA-DR (Fig. 5o). More importantly, after lenva treatment, there were abundant $CD8^+PD1^+$ Teffs surrounding the PCV ECs, with a notable increase in cell interactions (Fig. 5n,p). These findings suggested that targeting the tumor vasculature with lenva transitioned ECs into inflamed PCV ECs, thus boosting intratumoral lymphocyte influx and improving the response to ICIs.

Targeting tumor stroma involved in response to CASTLE therapy

Accumulating evidence is clear that CAFs subdue antitumor T cell immunity and interfere with immunotherapy[35]. Here, we categorized mesenchymal cells from scRNA-seq data into one pericyte cluster and four CAF clusters on the basis of transcriptional programs (Fig. 6a and Extended Data Fig. 7a,b). CAF1 cells expressed high levels of the myofibroblastic markers *POSTN* and *COL8A1* and were designated as myofibroblastic CAFs (myCAFs). CAF2 cells exhibited an inflammatory CAF (iCAF) phenotype, with expression of *CD34*, *FBLN1* and *FBLN5*, while CAF3 cells, which expressed *CD74*, *RELN* and *FBLN5*, were defined as antigen-presenting CAFs (apCAFs)[36] (Fig. 6a). CAF1 was enriched in protumor and ECM signaling, whereas CAF2 and CAF3 were abundant in proinflammatory pathways, with CAF3 exhibiting the strongest activities in lymphocyte migration and antigen presentation (Fig. 6b). Lenva+sint treatment was shown to increase the proportions of CAF2 and CAF3 (Fig. 6c), while upregulating genes and pathways that promoted immunogenicity (chemokine ligands, antigen presentation and the proinflammatory response) and downregulating collagen molecules and ECM pathways across the entire CAF population (Extended Data Fig. 7c,d). Specifically, lenva + sint treatment reduced the protumor and ECM pathways of CAF1, characterized by marked downregulation of collagen, TGFβ and matrix-remodeling related genes, with enhancement of proinflammatory effects (Fig. 6d,e and Extended Data Fig. 7e). We also identified positive correlations of the proportion of CAF1 with the proportion of $CD8^+PD1^{hi}$ Tex cells and the exhaustion score of $CD8^+PD1^{hi}$ T cells in the scRNA-seq data (Fig. 6f). NicheNet analysis revealed that CAF1 also mediated the exhaustion molecules of $CD8^+PD1^{hi}$ T cells through multiple ligands. Furthermore, this effect was attenuated by lenva treatment, as evidenced by decreased expression of both ligand and receptor genes (Fig. 6g). Consistently, interaction between CAF1 and $CD8^+PD1^{hi}$ T cells through collagen also decreased after lenva treatment (Extended Data Fig. 7f). We also noticed enhancements in the functionalities of CAF3 cells, particularly in terms of antigen presentation and the facilitation of lymphocyte migration, following lenva + sint treatment (Fig. 6h,i and Extended Data Fig. 7g). The CAF3 proportion positively correlated with $CD4^+CXCL13^+$ Tfh cells and $CD8^+PD1^{hi}$ Teffs in the scRNA-seq data (Extended Data Fig. 7h). Receptor–ligand pairings at the different time points suggested that CAF3 may attract more $CD8^+PD1^{hi}$ T cells to the tumor core region through the enhanced CXCL12–CXCR4 axis (Fig. 6j). The proportion of CAF3 was also positively associated with costimulatory receptor levels of $CD8^+PD1^{hi}$ T cells (Extended Data Fig. 7h), suggestive of T cell activation through MHC II modules. Regarding CAF2, we found an upregulated lymphocyte migration-related transcriptional signature after cryoablation on population level (Extended Data Fig. 7i,j) and positive correlations of the CAF2 proportion with the two $PD1^{hi}$ T cell populations and their effector scores (Extended Data Fig. 7k).

Recent studies reported that collagen deposition of myCAFs prevented Teffs from entering the tumor core[31]. Therefore, we performed spatial analysis to validate the spatial localization of these cells (Extended Data Fig. 7l,m). IMC data revealed an increase in apCAF and iCAF proportions following lenva + sint treatment (Fig. 6k,l and Extended Data Fig. 7n). Interestingly, although there was an increase in $CD8^+PD1^{hi}$ Teffs after cryoablation, these cells were restricted to the stroma surrounding the tumor cell nests and did not penetrate the tumor nests (Fig. 6k), exhibiting enhanced interaction with myCAFs (Fig. 6m,n). Following lenva + sint treatment, a large number of $CD8^+$ Teffs penetrated the tumor cell nest, further enhancing their interaction with the tumor cells and thereby exerting an antitumor effect (Fig. 6m,n). Taken together, these results suggested that targeting CAFs and their associated functions could yield therapeutics that enhance the response to immunotherapy in ICC.

Cryoablation plus lenva and anti-PD1 treatment delivered abscopal antitumor effects in an ICC model in female mice

We further validated the efficacy of cryoablation combined with lenva and anti-PD1 therapy in a KRAS-driven and p53-driven murine ICC model (Supplementary Fig. 1a). In this model, tumors on one flank were subjected to cryoablation, while contralateral tumors were retained to assess the abscopal effect (Fig. 7a). Notably, mice treated with the triple therapy exhibited significantly reduced tumor burden and extended survival compared to other groups (Fig. 7b–d). Flow cytometry analysis revealed that in tumor-draining lymph nodes (TdLNs), immune cell activation was evident in the two cryoablation-treated groups (cryo + anti-PD1 and cryo + lenva + anti-PD1), marked by an increase in DCs and $IFNγ^+$ and proliferating $CD8^+$ T cells (Fig. 7e–g and Supplementary Fig. 1b). Furthermore, within tumor tissues, the proportion of $MHC\ I^+$ EPs was elevated following cryoablation, indicating enhanced antigen-presenting capability (Fig. 7h and Supplementary Fig. 1c). Notably, only the triple-therapy group demonstrated a significant rise in intratumoral $IFNγ^+$ $CD8^+$ T cells (Fig. 7i,j). This effect might be linked to lenva-induced vascular normalization, supported by the increased presence of $SELP^+$ ECs (Fig. 7k), which likely promoted the intratumoral infiltration of Teffs.

Discussion

Our CASTLE-01 trial met the primary endpoint, demonstrating antitumor activity of cryoablation followed by lenva + sint and an ORR of 75% in participants with previously treated advanced or metastatic ICC. This trial confirms that localized cryoablation of one intrahepatic lesion, when combined with an ICI and lenva, elicits a systemic antitumor immune response in other lesions at distant sites in participants with ICC.

For more than a decade, there was no globally recognized standard of care for the management of advanced BTC that progressed on GemCis. The CASTLE regimen—a therapeutic combination comprising cryoablation, sint (an anti-PD1 antibody) and lenva—demonstrated pronounced clinical efficacy. The median PFS and OS were 16.8 months and 25.4 months, respectively, surpassing outcomes observed in prior studies evaluating cryoablation or anti-PD1 and lenva monotherapy[11,37–41]. The superior efficacy observed in our cohort can be attributed to the synergistic integration of all three modalities within the CASTLE regimen. Indeed, post hoc exploratory analyses of longitudinal single-cell

Fig. 7 | Cryoablation plus lenva and anti-PD1 treatment delivered superior abscopal antitumor effects in a female mouse ICC model. a, Schematic illustrating the evaluation of cryoablation plus lenva and anti-PD1 treatment effectiveness in an ectopic mouse ICC model. **b**, Differences in tumor growth between various treatment groups ($n = 6$ mice per group). Data are shown as the mean ± s.e.m. and were analyzed using a two-way analysis of variance (ANOVA). **c**, Tumor images on day 28 ($n = 6$ mice per group). **d**, OS in mice with ectopic ICC tumors ($n = 6$ mice per group). Data were analyzed using a log-rank test. **e**–**k**, Flow cytometry quantification of $CD11c^+$ DCs (**e**), $IFNγ^+CD8^+$ T cells (**f**) and $Ki67^+CD8^+$ T cells (**g**) from TdLNs and $MHC\ I^+$ EPs (**h**), $CD8^+$ T cells (**i**), $IFNγ^+CD8^+$ T cells (**j**) and $SELP^+$ ECs (**k**) from tumors of mice with different treatment groups. Mice were killed on day 21 ($n = 5$ mice per group). Data are shown as the mean ± s.d. and were analyzed using a one-way ANOVA. **l**, Schematic illustration of the cellular composition dynamics and potential therapeutic mechanism of cryoablation followed by lenva + sint.

https://doi.org/10.1038/s43018-025-01058-2

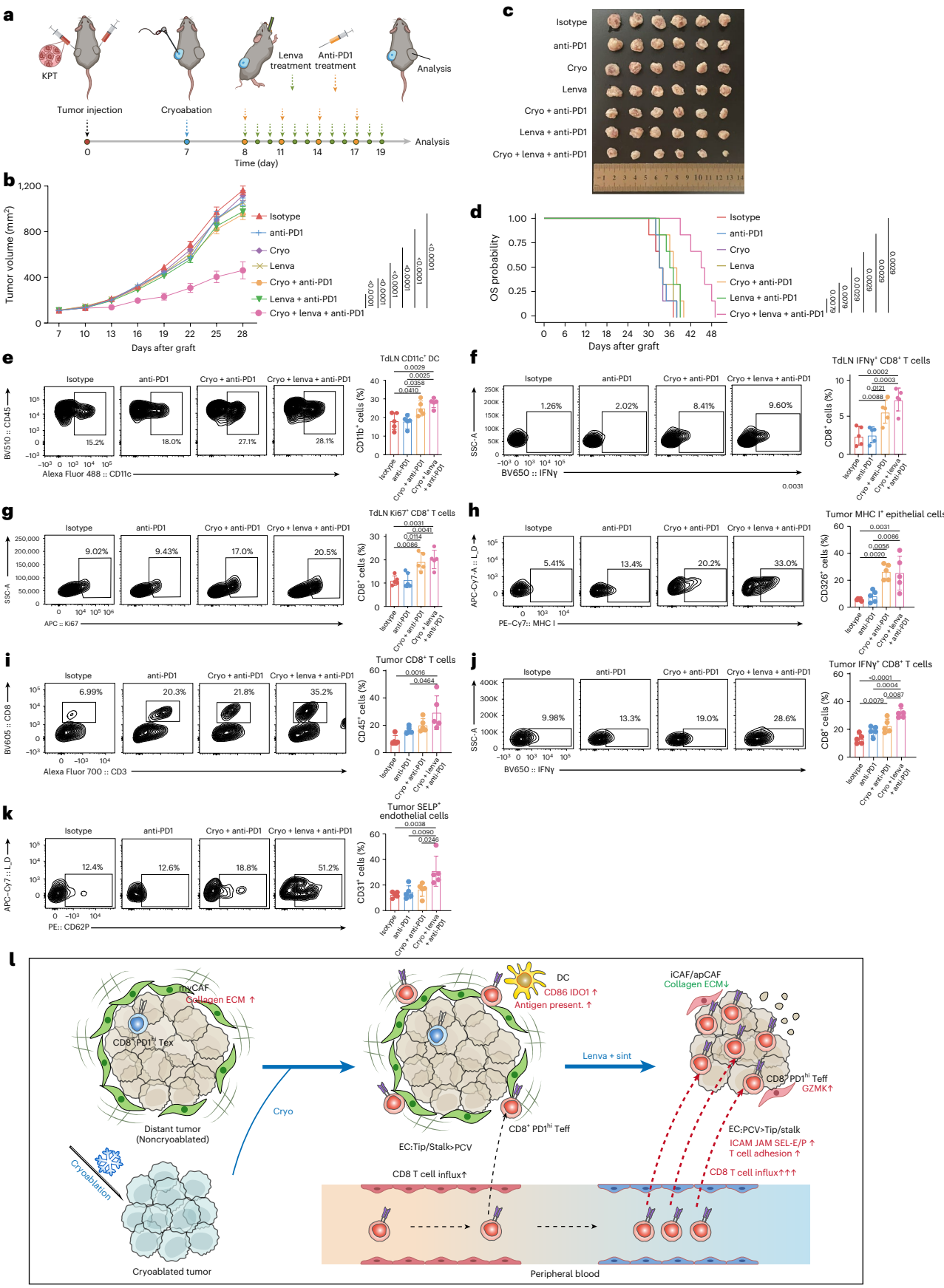

sequencing and IMC datasets indicated that cryoablation induced increased $CD8^+PD1^{hi}$ Teff infiltration into distant tumors; however, the increased numbers of $CD8^+PD1^{hi}$ Teffs after cryoablation were restricted to the stroma surrounding the tumor cell nest and did not penetrate the nest. Large numbers of $CD8^+$ Teffs infiltrated the tumor cell nest only after lenva treatment, where they killed the tumor cells. The mechanism underlying the combination of cryoablation, ICI and lenva was also confirmed by in vivo animal study. Therefore, these findings underscore the critical and complementary roles of each component in the CASTLE regimen, wherein cryoablation primes the immune microenvironment, sint sustains T cell activity and lenva enhances Teff trafficking and tumor cell targeting.

In this study, we observed an increase in $CD8^+PD1^{hi}$ Teff infiltration into distant tumors, which may have been associated with the cryoablation-induced increase in tumor immunogenicity, antigen presentation and DC activation, highlighting the indispensable role of cryoablation in this regimen (Fig. 7l). Another central finding from lineage tracing of PBMCs revealed that many newly emerged $CD8^+PD1^{hi}$ Teffs appeared in the peripheral blood after cryoablation but only infiltrated tumors after treatment with lenva + sint, suggesting that this process involves EC regulation. Indeed, following lenva treatment, there were increased numbers of PCV ECs expressing high levels of molecules related to lymphocyte adhesion and migration, as well as a variety of genes implicated in IFN-regulated inflammation and antigen processing. Therefore, our findings suggest that lenva transitioned ECs into inflamed PCV ECs, thereby boosting intratumoral lymphocyte influx. In addition to ECs, accumulating evidence is clear that CAFs subdue antitumor T cell immunity and interfere with immunotherapy[35]. Cholangiocarcinoma is characterized by a strong desmoplastic stroma surrounding cancer cells[42]. In this study, we found that the increased numbers of $CD8^+PD1^{hi}$ Teffs after cryoablation were restricted to the stroma surrounding the tumor cell nest but did not penetrate the nest, showing enhanced interaction with myCAFs. However, after lenva + sint treatment, large numbers of $CD8^+$ Teffs infiltrated the tumor cell nest, further enhancing their interaction with the tumor cells. This antitumor effect suggested that targeting the tumor stroma, especially CAFs and their associated functions, may yield therapeutics that enhance the response to immunotherapy in ICC.

This trial has several limitations. First, the small sample size and the single-arm study design necessitate confirmation of the preliminary antitumor activity results in prospective, randomized controlled trials. Second, objective response was not assessed by independent central review, which might have led to an overestimation of the antitumor activity results. Third, GemCis plus ICI is a recently proven first-line treatment for advanced BTC. Whether the CASTLE regimen is effective in participants who have progressed after GemCis plus ICI therapy requires further verification. Therefore, a new randomized controlled trial that evaluated the efficacy of cryoablation combined with lenva plus anti-PD1 compared to FOLFOX in participants with advanced ICC who have progressed after GemCis+ICI is now ongoing (NCT06860477).

In conclusion, the CASTLE-01 trial suggests that cryoablation followed by lenva + sint represents a promising approach for the treatment of advanced or metastatic ICC. These findings also support the notion that cryoablation-induced local antitumor immunity elicits a systemic antitumor response at distant sites (abscopal effect) when combined with lenva and an ICI.

Methods

Study design and participants

CASTLE-01 was an open-label, single-arm, phase 2 trial that followed the Consolidated Standards of Reporting Trials (CONSORT) reporting guidelines[43]. The trial was performed in accordance with the principles of Good Clinical Practice and the Declaration of Helsinki. The study protocol and amendments were approved by the ethics committee of the Fudan University Shanghai Cancer Center (approval no. 1905201-11). All participants provided written, informed consent for participation and publication of potentially identifying clinical information before enrollment (ClinicalTrials.gov NCT05010668, preregistered at August 11, 2021). From the enrollment of the first participant on August 24, 2021, to the enrollment of the last participant on May 12, 2023, a total of 28 participants were enrolled. Eligible participants were 18 years or older with histologically confirmed ICC before enrollment. Other eligibility criteria included the following: ECOG performance status score 0–2, disease that was not amenable to potentially curative liver transplantation or resection, progression of disease on at least one line of chemotherapy, including GemCis, adequate organ and marrow function and no history of chronic autoimmunity or inflammatory bowel disease. All enrolled participants had to have at least two distinct lesions, with one intrahepatic lesion amenable to cryoablation and the remaining lesion(s), either intrahepatic or extrahepatic, designated as the target lesion(s) for response assessment in accordance with the RECIST version 1.1 using spiral computed tomography (CT) or magnetic resonance imaging (MRI). The cryoablated lesion was excluded from response assessment. Figure 1b illustrates the treatment strategy and discontinuation profile of the 28 enrolled participants. The study protocol is included in the Supplementary Information.

Procedures

All participants received the CASTLE regimen comprising cryoablation, sint and lenva. Cryoablation was conducted on day 0. Administration of lenva at 8 mg per day (body weight < 60 kg) or 12 mg per day (body weight ≥ 60 kg) plus sint at 200 mg every 3 weeks was initiated at 2 weeks after cryoablation and continued for 24 months from the first dose of lenva + sint or until the development of progressive disease confirmed by RECIST version 1.1 or treatment intolerance, whichever occurred first. All participants underwent partial cryoablation. The selection of the lesion subjected to cryoablation was based on technical factors, including access and proximity to major vessels and adjacent hollow viscera. All cryoablations were performed using the Co-Ablation System from Hygea Medical Technology. On the basis of the size and location of the tumor, cryoprobes were percutaneously inserted into the center of the tumor mass under ultrasound guidance. After the position of the probe was confirmed, the temperature at the tip of the probe was lowered to −196 °C. Tumors were frozen for 25 min and thawed to 80 °C for 5 min. Two freeze–thaw cycles were routinely used.

Endpoints

The primary endpoint was the investigator-assessed ORR, which was based on RECIST version 1.1. The cryoablation-treated lesion was not included in the treatment response evaluation and was designated as a nontarget lesion. The secondary endpoints were safety, investigator-assessed DCR, DOR, PFS and OS. ORR was defined in accordance with RECIST version 1.1 as the proportion of participants who achieved a confirmed best overall response of CR or PR. DCR was defined as the proportion of participants who achieved CR, PR or SD. DOR was defined as the time from the first recorded CR or PR to disease progression or death for participants with CR or PR. PFS was defined as the time from enrollment to the first recorded imaging of disease progression or death from any cause, whichever occurred first. OS was defined as the time from enrollment to recorded death from any cause. TTR was observed as an exploratory endpoint in participants with post hoc response, defined as the time from enrollment to the first recorded, investigator-assessed CR or PR for confirmed participants. We also conducted exploratory analyses to examine the potential association of treatment response with a variety of immunologic parameters.

Clinical assessments

Radiological evaluation was performed using CT or MRI at baseline and at 6-week intervals following the initial administration of lenva + sint. Tumor responses determined using RECIST version 1.1 criteria

were specified by investigators in the study protocol and reported with an exact 95% CI. CR or PR was considered to be confirmed only if the criteria for each were met at a subsequent time point (4–6 weeks later). All AEs and serious AEs occurring within 30 days of the last dose were reported in accordance with the National Cancer Institute Common Terminology Criteria for AEs version 5.0. The safety population was defined as all participants who received at least one dose of sint and/or lenva.

Sample collection and single-cell dissociation

All sample collection followed standard clinical practices. Site-matched liver tumor biopsies from the same cryoablation-untreated lesion were obtained at three time points: baseline biopsy, 2 weeks after cryoablation and after the first two doses of lenva + sint. Tumor biopsies were always collected from the same prespecified lesion to limit sampling bias. Tumor lesions were punctured by 16-gauge needles twice or thrice at each sampling time. Tissue samples were processed within 2 h for single-cell sequencing. Alternatively, samples were snap-frozen or paraffin-embedded. PBMCs were isolated with Lymphoprep (StemCell Technologies), cryopreserved and thawed before processing. For single-cell dissociation, tissue biopsies were minced and digested with 300 U per ml collagenase II and 100 U per ml collagenase IV (Worthington) for 30 min at 37 °C with shaking. Tissue was filtered through a 70-µm strainer, centrifuged and treated with red blood cell lysis buffer (Miltenyi Biotec). After PBS wash, pellets were filtered through a 35-µm strainer.

scRNA-seq and scTCR-seq library preparation and sequencing

Single-cell transcriptomes and TCR V(D)J libraries were generated using the Chromium Next-GEM single-cell 5′ kit v2 and the Chromium single-cell human TCR amplification kit (10x Genomics). Briefly, cells were concentrated to approximately 1,000 cells per µl and loaded into each channel to generate single-cell gel beads in emulsion (GEMs). After reverse transcription and cell barcoding, GEMs were broken and complementary DNA (cDNA) was isolated, purified and amplified by PCR. The amplified barcoded cDNAs were then used to generate 5′ transcriptome libraries and TCR V(D)J libraries. All single-cell transcriptomes and TCR V(D)J libraries were sequenced using Illumina NovaSeq 6000 platform.

scRNA-seq data processing and clustering

scRNA-seq data were processed using CellRanger (version 6.0.1) for GRCh38 alignment, barcode and unique molecular identifier (UMI) processing and gene–cell matrix generation. Quality control was performed by filtering out cells with UMI or gene counts outside the 1st–95th percentiles, as well as those with high mitochondrial (>15%), ribosomal (>30%) or hemoglobin (>5%) gene expression. Potential doublets were identified and removed using scDblFinder. We then used Seurat (version 4.3.0) to process the UMI count matrix and integrated all cells on the basis of sample identifier by Harmony (version 1.0)[44]. To define the major clusters, we split the cells according to their commonly used markers (*CD4* for CD4 T cells, *CD8A* for CD8 T cells, *SLC4A10* for mucosal-associated invariant T cells, *KLRC1* for natural killer cells, *CD79A* for B and plasma cells, *VWF* for ECs, *COL1A1* for mesenchymal cells, *KRT19* for EPs, *APOC3* for hepatocytes and *S100A9* and *CD68* for myeloid cells) (Extended Data Fig. 2). For the major immune clusters ($CD8^+$ T cells, $CD4^+$ T cells and myeloid cells), participant data were excluded from paired subpopulation proportion calculations if a sample had fewer than 30 cells. Similarly, for the major mesenchymal clusters (ECs and fibroblasts), a cutoff of fewer than 20 was used.

Identification of marker genes and generation of signatures

Marker gene identification and signature generation were performed using Seurat's 'FindAllMarkers' function to characterize cellular populations. Signatures for EP1, PCV, stalk and tip were derived from top differentially expressed genes (ranked by average $\log_2$ fold change; Supplementary Table 7), while others were obtained from previous studies (Supplementary Table 8) or MsigDB (version 7.5.1). For PFS and OS negative signature generation, genes in the bulk RNA-seq meta-cohort were assessed for linear association with PFS or OS using Cox proportional hazards models. Those with HR > 1 and $P < 0.05$ were incorporated into negative PFS or OS signatures. Signature scores were calculated with Seurat's AddModuleScore in scRNA-seq and ssGSEA from GSVA (version 1.40.1) in bulk RNA-seq.

Cell differentiation trajectory inference

To infer the differentiation trajectory of cell clusters, we used both the R-based Monocle (version 2.20.0)[45] and the Python-based ScVelo (version 0.2.2)[46]. For Monocle, we calculated the pseudotime of each cell using the 'DDRTree' method. To predict the cell differentiation direction, loom files were first generated from their BAM files using Velocyto (version 0.17.17)[47]. ScVelo was then applied for further pseudotime estimation.

Copy-number variation (CNV) analysis of malignant cells

Copy-number instability was assessed with the R-based inferCNV (version 1.10.1), which is designed to infer CNV of scRNA-seq data. An adjacent normal liver sample was set as the reference normal sample.

Cell-to-cell communication of scRNA-seq data

The analysis of intercellular interactions among cell clusters was efficiently carried out using CellChat (version 1.1.3)[48], which was designed to infer biologically meaningful cell-to-cell communication patterns derived from scRNA-seq data. We also applied NicheNet (version 1.1.1)[49] to identify potential receptor–ligand pairs and their regulatory potential on the basis of the expression of genes of interest within the target clusters.

scTCR-seq data analysis

CellRanger (version 6.0.1; 10x Genomics) was applied to align TCR-seq reads to GRCh38 and assemble TCR sequences. Clonotypes were defined on the basis of unique CDR3α/β nucleotide sequences from high-confidence cells with valid barcodes and unambiguous chain assignments. Persistent clones in T4 meant clones preexisting in T4 at baseline and being persistent after both cryoablation and lenva + sint treatment (Fig. 3j,k). Novel clones in T4 were defined as intratumoral clones only emerged after lenva + sint treatment but absent both at baseline and after cryoablation (Fig. 3l–q). We also applied the STARTRAC algorithm (version 0.1.0)[50] to calculate the clonal expansion and transition score.

IMC section preparation

We collected 15 paraffin-embedded and formalin-fixed (FFPE) samples from five participants at three time points. Each tissue sample was verified by pathological examinations and subjected to H&E staining to select the ROIs by a pathological expert. In total, we chose 88 ROIs to be scanned by IMC. FFPE sections (4 µm) were baked at 68 °C for 1 h, cooled naturally and washed twice with PBS-TB (PBS with 0.5% Tween-20 and 1% BSA; Sigma-Aldrich). After blocking with SuperBlock (Thermo Fisher Scientific), sections were washed and incubated overnight at 4 °C with a metal-labeled antibody cocktail. The final antibody panel is detailed in Supplementary Table 9. After overnight incubation, sections were washed thrice with PBS-TB. Nuclei were labeled with 1.25 µM Intercalator-Ir (Fluidigm) in PBS-TB for 30 min at room temperature, followed by two PBS-TB washes and one double-distilled H_2O wash.

IMC image preprocessing and downstream analysis

Multiplexed images were acquired using an IMC instrument (Fluidigm, Hyperion). The IMC analysis pipeline included spillover compensation, image denoising, contrast enhancement and cell segmentation.

Segmentation was performed using regionprops (Matlab) to identify connected components. Single-cell masks were generated with CellProfiler (version 4.2.8). Marker expression was range-normalized to the 99th percentile per channel and batch-corrected with Harmony. Processed data were used for cell annotation and downstream analyses. To identify pairwise cellular interactions, we performed a permutation-test-based analysis of spatial single-cell interactions among all cell types within each ROI using the 'test_interactions' method in imcRtools (version 1.0.2).

Bulk RNA-seq

RNA was extracted from biopsy tissues using the AllPrep DNA/RNA mini kit (Qiagen). Libraries from 46 qualified samples were constructed and sequenced on a NovaSeq 6000 (Illumina). We applied FASTQ[51] to examine the quality of the raw sequencing reads and HISAT2 (ref. 52) to map reads to GRCh38. Read counts were calculated using HTseq[53].

Whole-exome sequencing (WES)

DNA was extracted from 25 qualified matched pairs of biopsy tissues and peripheral blood samples using the AllPrep DNA/RNA mini kit (Qiagen) for library construction. WES was performed on an Illumina NovaSeq 6000. WES data were preprocessed according to GATK best practices workflow and aligned to GRCh38. Somatic variants were called by Mutect2, Varscan2 and TNscope and annotated using Ensembl variant effect predictor. Somatic mutations were confirmed if identified by at least two of the three variant callers. CNV was calculated using CNVkit. TMB > 10 was classified as TMB-high[54]. Microsatellite instability (MSI) status was determined with a cutoff value of 3.5 (ref. 55) by MSIsensor.

Bulk TCR-seq data processing and analysis

We performed bulk TCR-seq on frozen PBMC samples from 13 participants at three time points. Total RNA was extracted using the AIIPrep DNA/RNA mini kit (Qiagen). Reverse transcription was performed to acquire the first-strand cDNA, which was then amplified and purified for library construction. The final libraries were evaluated using Qubit 4 Fluorometers (Thermo Fisher Scientific), and 2× 150-bp paired-end sequencing was conducted using the NovaSeq 6000 (Illumina). Sequences were processed and analyzed using the MiXCR method (version 4.3.2).

Pathology assessment

Histopathological lymphocyte infiltration was assessed on H&E-stained sections by pathologists blinded to clinical data. Intratumoral lymphocytes were quantified as the percentage of tumor epithelial nests containing infiltrating mononuclear cells[56,57]. Stromal lymphocytes were defined as the percentage of stromal area with lymphocytic infiltration. TLSs were identified as organized lymphoid aggregates with germinal centers[58].

Animal experiments

All the animals in this study was applied with C57BL/6 mice (female, 6–8 weeks of age), which were housed in a specific-pathogen-free facility at Shanghai Yishang Biotechnology. All animal breeding and experiments were conducted in accordance with institutional guidelines and were approved by the Institutional Animal Care and Use Committee guidelines (IACUC-2024-Mi-090). Animals were removed from the study and killed if any signs of pain and distress were detected or if the tumor volume reached 2,000 mm^3. The maximal tumor size was not exceeded in all reported studies.

KRAS/p53 murine ICC models were established through hydrodynamic tail-vein injection of plasmids at a 10:1 transposon-to-transposase ratio (25 µg of pT3-EF1a-KRASG12D and 25 µg of PX330-CRISPR/Cas9 sgRNA-p53), in a volume equivalent to 10% body weight injected within 6–8 s. The KPT cell line was derived in vitro from this model and was gifted from Q. Gao (Zhongshan Hospital, Fudan University).

For ectopic implantation of murine ICC model, 1×10^6 KPT cells suspended in 200 µl of PBS were injected subcutaneously into the both flanks of C57BL/6 mice. When performing the cryoablation on day 7, an ablation probe (17 gauge, Hygea Medical Technology) was inserted into the center of tumor. The tumor was macroscopically frozen at −50 ± 10 °C for 120 s, while leaving healthy tissue intact. Then, the tumor was thawed using ethyl alcohol at 70 °C for 120 s. Anti-PD1 and lenva treatment started at the day after cryoablation. These mice received intraperitoneal injection of anti-mouse PD1 antibody (BioXCell, BE0146; 10 mg kg^{-1}) every 3 days, oral administration of lenva (Selleck, S1164, 3 mg kg^{-1}) every day, a combination of both or their respective isotype controls (BioXCell, BP0089; Selleck, S6703). The uncryoablated lesions were assessed and measured. At the end of the treatment period, tumors were isolated for further experiments.

Flow cytometry

For flow cytometry, ectopic ICC tumor tissues were collected and processed into single-cell suspensions. Cells were first stained with a viability dye (BioLegend, 423105) to exclude dead cells. After washing, Fc receptors were blocked using anti-CD16/32 antibody (BioLegend, 101302), followed by specific antibody staining on ice for 30 min. The stained cells were analyzed on a BD LSRFortessa X-20 flow cytometer (BD Pharmingen) and data were processed using FlowJo software (version 10.8.1). The antibodies used for this flow cytometry are listed in Supplementary Table 9.

Immunofluorescence staining

Multiplex immunofluorescence staining was performed on 3-µm-thick FFPE tissue sections. After deparaffinization, heat-induced antigen retrieval was conducted using Tris–EDTA buffer (pH 9.0). Sections were blocked and then incubated overnight at 4 °C with primary antibodies. Following PBS-T (0.5%) washes, sections were incubated with appropriate species-matched secondary antibodies conjugated to fluorescent dyes. The primary antibodies were listed in Supplementary Table 9. Whole-slide imaging was performed at ×40 magnification using the Vectra Polaris automated quantitative pathology imaging system, with subsequent image analysis conducted using HALO image platform (Indica Labs) and ImageJ software (National Institutes of Health).

Statistics and reproducibility

Sample size was calculated using a binomial exact single-stage phase 2 design. Considering that the ORR of the standard second-line treatment regimen FOLFOX is 5% and the phase 2 study of lenva plus pembrolizumab reported an ORR of 10%, the null hypothesis was that an ORR rate of 10% cryoablation followed by lenva + sint would not be worthy of further evaluation in this population. The alternative hypothesis was that an ORR rate of 30% for the combination of cryoablation followed by lenva + sint would be promising, with 25 participants providing >80% power to detect this increase in ORR at a two-sided 5% significance level. The proportions and 95% CIs for ORR were calculated using the Clopper–Pearson method. The Kaplan–Meier method was used to summarize DOR, TTR, PFS and OS. Median values of PFS, OS, TTR and 95% CI were calculated using the Brookmeyer–Crowley method. Descriptive safety analyses are presented in a tabular format with the appropriate summary statistics. Efficacy endpoints were analyzed in the intention-to-treat population; safety analyses were conducted in participants who received at least one dose of sint and/or lenva. When performing correlation analysis on the basis of single-cell data, if two variables exhibited a linear relationship, normal distribution and homoscedasticity, the Pearson correlation test was used. If not, the Spearman correlation test was applied instead. Flow cytometry experiments and pathology assessment were conducted in a blinded fashion, whereas other experiments were not, as the experiments were conducted and

analyzed by the same researchers. Mouse tumor experiments were randomized such that the groups had no differences in mean body weight at the start of the experiment. No data were excluded from the analyses. Data distribution was assumed to be normal but this was not formally tested. All statistical analyses were conducted using R software version 4.3.0 and GraphPad Prism version 8.4.0.

Reporting summary

Further information on research design is available in the Nature Portfolio Reporting Summary linked to this article.

Data availability

The study protocol is available in the Supplementary Information file. Deidentified individual participant data reported in the paper will be shared under data use agreements upon reasonable request. The sequencing data generated in this study (scRNA, scTCR-seq, WES, bulk RNA-seq and bulk TCR-seq data) were deposited into the Genome Sequence Archive (GSA) in the National Genomics Data Center, China National Center for Bioinformation/Beijing Institute of Genomics, Chinese Academy of Sciences (https://ngdc.cncb.ac.cn/gsa/), under project accession numbers PRJCA025263, PRJCA025324, PRJCA025505 and PRJCA025506. All sequencing data generated in this study are available under the terms of a Data Use Agreement that addresses the privacy and security requirements for safeguarding the data and may only be used for research purposes. Response to access requests is typically expected within 2 weeks and data will remain available to approved requesters for 1 month. For detailed instructions on how to request access, please refer to the GSA's guidelines. Previously published bulk RNA-seq data of IMbrave150 and GO30140 cohorts (EGAC00001002314) are available upon request through the European Genome–Phenome Archive. The remaining data are available within the article and its Supplementary Information or from the corresponding author on request. Source data are provided with this paper.

Code availability

No new algorithms were developed for this study. All code generated for analysis is publicly available from Github (https://github.com/SJ-GU/CASTLE-01).

References

1. Shaib, Y. H., Davila, J. A., McGlynn, K. & El-Serag, H. B. Rising incidence of intrahepatic cholangiocarcinoma in the United States: a true increase? *J. Hepatol.* **40**, 472–477 (2004).
2. Valle, J. et al. Cisplatin plus gemcitabine versus gemcitabine for biliary tract cancer. *N. Engl. J. Med.* **362**, 1273–1281 (2010).
3. Oh, D. Y., et al. Durvalumab plus gemcitabine and cisplatin in advanced biliary tract cancer. *NEJM Evid.* **1**, EVIDoa2200015 (2022).
4. Kelley, R. K. et al. Pembrolizumab in combination with gemcitabine and cisplatin compared with gemcitabine and cisplatin alone for patients with advanced biliary tract cancer (KEYNOTE-966): a randomised, double-blind, placebo-controlled, phase 3 trial. *Lancet* **401**, 1853–1865 (2023).
5. Valle, J. W., Kelley, R. K., Nervi, B., Oh, D. Y. & Zhu, A. X. Biliary tract cancer. *Lancet* **397**, 428–444 (2021).
6. Lamarca, A., Hubner, R. A., David Ryder, W. & Valle, J. W. Second-line chemotherapy in advanced biliary cancer: a systematic review. *Ann. Oncol.* **25**, 2328–2338 (2014).
7. Lowery, M. A. et al. Comprehensive molecular profiling of intrahepatic and extrahepatic cholangiocarcinomas: potential targets for intervention. *Clin. Cancer Res.* **24**, 4154–4161 (2018).
8. Mosele, M. F. et al. Recommendations for the use of next-generation sequencing (NGS) for patients with advanced cancer in 2024: a report from the ESMO Precision Medicine Working Group. *Ann. Oncol.* **35**, 588–606 (2024).
9. Dong, L. et al. Proteogenomic characterization identifies clinically relevant subgroups of intrahepatic cholangiocarcinoma. *Cancer Cell* **40**, 70–87 (2022).
10. Lamarca, A. et al. Second-line FOLFOX chemotherapy versus active symptom control for advanced biliary tract cancer (ABC-06): a phase 3, open-label, randomised, controlled trial. *Lancet Oncol.* **22**, 690–701 (2021).
11. Kim, R. D. et al. A phase 2 multi-institutional study of nivolumab for patients with advanced refractory biliary tract cancer. *JAMA Oncol.* **6**, 888–894 (2020).
12. Erinjeri, J. P. & Clark, T. W. Cryoablation: mechanism of action and devices. *J. Vasc. Interv. Radiol.* **21**, S187–S191 (2010).
13. Chin, J. L., Al-Zahrani, A. A., Autran-Gomez, A. M., Williams, A. K. & Bauman, G. Extended followup oncologic outcome of randomized trial between cryoablation and external beam therapy for locally advanced prostate cancer (T2c–T3b). *J. Urol.* **188**, 1170–1175 (2012).
14. Wang, C. et al. Multicenter randomized controlled trial of percutaneous cryoablation versus radiofrequency ablation in hepatocellular carcinoma. *Hepatology* **61**, 1579–1590 (2015).
15. Toi, M. et al. Non-surgical ablation for breast cancer: an emerging therapeutic option. *Lancet Oncol.* **25**, e114–e125 (2024).
16. Shen, L. et al. Cryoablation combined with transarterial infusion of pembrolizumab (CATAP) for liver metastases of melanoma: an ambispective, proof-of-concept cohort study. *Cancer Immunol. Immunother.* **69**, 1713–1724 (2020).
17. Yakkala, C., Denys, A., Kandalaft, L. & Duran, R. Cryoablation and immunotherapy of cancer. *Curr. Opin. Biotechnol.* **65**, 60–64 (2020).
18. Llovet, J. M. et al. Locoregional therapies in the era of molecular and immune treatments for hepatocellular carcinoma. *Nat. Rev. Gastroenterol. Hepatol.* **18**, 293–313 (2021).
19. Shen, L., et al. Size selection of intrahepatic lesions for cryoablation contributes to abscopal effect and long-term survival in patients with liver metastatic melanoma receiving PD-1 blockade therapy. *Cancer Immunol. Immunother.* **73**, 68 (2024).
20. Waitz, R. et al. Potent induction of tumor immunity by combining tumor cryoablation with anti-CTLA-4 therapy. *Cancer Res.* **72**, 430–439 (2012).
21. Waitz, R., Fassò, M. & Allison, J. P. CTLA-4 blockade synergizes with cryoablation to mediate tumor rejection. *Oncoimmunology* **1**, 544–546 (2012).
22. Campbell, M. T. et al. Pilot study of tremelimumab with and without cryoablation in patients with metastatic renal cell carcinoma. *Nat. Commun.* **12**, 6375 (2021).
23. Mooradian, M. J. et al. Cryoablation and post-progression immune checkpoint inhibition in metastatic melanoma: a phase II trial. *Nat. Commun.* **15**, 7357 (2024).
24. den Brok, M. H. et al. Efficient loading of dendritic cells following cryo and radiofrequency ablation in combination with immune modulation induces anti-tumour immunity. *Br. J. Cancer* **95**, 896–905 (2006).
25. Benzon, B. et al. Combining immune check-point blockade and cryoablation in an immunocompetent hormone sensitive murine model of prostate cancer. *Prostate Cancer Prostatic Dis.* **21**, 126–136 (2018).
26. Alshebremi, M. et al. Functional tumor cell-intrinsic STING, not host STING, drives local and systemic antitumor immunity and therapy efficacy following cryoablation. *J. Immunother. Cancer* **11**, e006608 (2023).
27. Gu, C. et al. Cryoablation triggers type I interferon-dependent antitumor immunity and potentiates immunotherapy efficacy in lung cancer. *J. Immunother. Cancer* **12**, e008386 (2024).

28. Shewarega, A. et al. Effect of incomplete cryoablation and matrix metalloproteinase inhibition on intratumoral CD8⁺ T-cell infiltration in murine hepatocellular carcinoma. *Radiology* **310**, e232365 (2024).
29. Lee, M. S. et al. Atezolizumab with or without bevacizumab in unresectable hepatocellular carcinoma (GO30140): an open-label, multicentre, phase 1b study. *Lancet Oncol.* **21**, 808–820 (2020).
30. Galle, P. R. et al. Patient-reported outcomes with atezolizumab plus bevacizumab versus sorafenib in patients with unresectable hepatocellular carcinoma (IMbrave150): an open-label, randomised, phase 3 trial. *Lancet Oncol.* **22**, 991–1001 (2021).
31. Cords, L. et al. Cancer-associated fibroblast phenotypes are associated with patient outcome in non-small cell lung cancer. *Cancer Cell* **42**, 396–412 (2024).
32. Schmittnaegel, M. et al. Dual angiopoietin-2 and VEGFA inhibition elicits antitumor immunity that is enhanced by PD-1 checkpoint blockade. *Sci. Transl. Med.* **9**, eaak9670 (2017).
33. Goveia, J. et al. An integrated gene expression landscape profiling approach to identify lung tumor endothelial cell heterogeneity and angiogenic candidates. *Cancer Cell* **37**, 21–36 (2020).
34. Hua, Y. et al. Cancer immunotherapies transition endothelial cells into HEVs that generate TCF1(+) T lymphocyte niches through a feed-forward loop. *Cancer Cell* **40**, 1600–1618 (2022).
35. Chua, Z. M., Tajebe, F., Abuwarwar, M. & Fletcher, A. L. Differential induction of T-cell tolerance by tumour fibroblast subsets. *Curr. Opin. Immunol.* **86**, 102410 (2024).
36. Kieffer, Y. et al. Single-cell analysis reveals fibroblast clusters linked to immunotherapy resistance in cancer. *Cancer Discov.* **10**, 1330–1351 (2020).
37. Piha-Paul, S. A. et al. Efficacy and safety of pembrolizumab for the treatment of advanced biliary cancer: results from the KEYNOTE-158 and KEYNOTE-028 studies. *Int. J. Cancer* **147**, 2190–2198 (2020).
38. Ueno, M. et al. Phase 2 study of lenvatinib monotherapy as second-line treatment in unresectable biliary tract cancer: primary analysis results. *BMC Cancer* **20**, 1105 (2020).
39. Ueno, M. et al. Phase I/II study of nivolumab plus lenvatinib for advanced biliary tract cancer (JCOG1808/NCCH1817, SNIPE). *ESMO Open* **9**, 103919 (2024).
40. Wang, Y. et al. Lenvatinib beyond first-line therapy in patients with advanced biliary tract carcinoma. *Front. Oncol.* **12**, 785535 (2022).
41. Amini, A. & Gamblin, T. C. Palliation: treating patients with inoperable biliary tract and primary liver tumors. *Surg. Oncol. Clin. N. Am.* **23**, 383–397 (2014).
42. Guedj, N. et al. Prognostic value of desmoplastic stroma in intrahepatic cholangiocarcinoma. *Mod. Pathol.* **34**, 408–416 (2021).
43. Schulz, K. F., Altman, D. G. & Moher, D. CONSORT 2010 statement: updated guidelines for reporting parallel group randomised trials. *Brit. Med. J.* **340**, c332 (2010).
44. Korsunsky, I. et al. Fast, sensitive and accurate integration of single-cell data with Harmony. *Nat. Methods* **16**, 1289–1296 (2019).
45. Qiu, X. et al. Single-cell mRNA quantification and differential analysis with Census. *Nat. Methods* **14**, 309–315 (2017).
46. Bergen, V., Lange, M., Peidli, S., Wolf, F. A. & Theis, F. J. Generalizing RNA velocity to transient cell states through dynamical modeling. *Nat. Biotechnol.* **38**, 1408–1414 (2020).
47. La Manno, G. et al. RNA velocity of single cells. *Nature* **560**, 494–498 (2018).
48. Jin, S. et al. Inference and analysis of cell-cell communication using CellChat. *Nat. Commun.* **12**, 1088 (2021).
49. Browaeys, R., Saelens, W. & Saeys, Y. NicheNet: modeling intercellular communication by linking ligands to target genes. *Nat. Methods* **17**, 159–162 (2020).
50. Zhang, L. et al. Lineage tracking reveals dynamic relationships of T cells in colorectal cancer. *Nature* **564**, 268–272 (2018).
51. Chen, S., Zhou, Y., Chen, Y. & Gu, J. fastp: an ultra-fast all-in-one FASTQ preprocessor. *Bioinformatics* **34**, i884–i890 (2018).
52. Kim, D., Langmead, B. & Salzberg, S. L. HISAT: a fast spliced aligner with low memory requirements. *Nat. Methods* **12**, 357–360 (2015).
53. Anders, S., Pyl, P. T. & Huber, W. HTSeq—a Python framework to work with high-throughput sequencing data. *Bioinformatics* **31**, 166–169 (2015).
54. Cao, J. et al. Intrahepatic cholangiocarcinoma: genomic heterogeneity between eastern and western patients. *JCO Precis. Oncol* **4**, 557–569 (2020).
55. Niu, B. et al. MSIsensor: microsatellite instability detection using paired tumor-normal sequence data. *Bioinformatics* **30**, 1015–1016 (2014).
56. Denkert, C. et al. Tumor-associated lymphocytes as an independent predictor of response to neoadjuvant chemotherapy in breast cancer. *J. Clin. Oncol.* **28**, 105–113 (2010).
57. Loi, S. et al. Prognostic and predictive value of tumor-infiltrating lymphocytes in a phase III randomized adjuvant breast cancer trial in node-positive breast cancer comparing the addition of docetaxel to doxorubicin with doxorubicin-based chemotherapy: BIG 02-98. *J. Clin. Oncol.* **31**, 860–867 (2013).
58. Helmink, B. A. et al. B cells and tertiary lymphoid structures promote immunotherapy response. *Nature* **577**, 549–555 (2020).

Acknowledgements

We thank all participants and their families for participating in this study. This work was supported by the National Natural Science Foundation of China (82025035 and 82230122 to P.W., 82104612 to Y. L.), Discipline Breakthrough Precursor Project of the Ministry of Education of China (to P.W.), the National Key Research and Development Program of China (2023YFC2414000 to P.W.) and Shanghai Science and Technology Committee Program (23Y11902600 to Y.L.). The funders had no role in the study design, collection, data analysis or interpretation of the data, in the writing of the report or in the decision to submit the article for publication.

Author contributions

Conceptualization, P.W. Methodology: S.G. and Q.L. Software, S.G., Q.L. and F.L. Formal analysis, S.G. and Q.L. Writing—original draft, S.G. Writing—review and editing, P.W. and Y.L. Visualization, S.G. Funding acquisition, P.W. and Y.L. Participant enrollment and management, Y.L., Z.M., Z.N., L.X. and P.W. Sample collection and sampling, S.G., Q.L., Y.L., L.Q., K.C., J.L., Y.Z., R.Z., Y.H., Y.W., Y.L. and P.W. Supervision, Y.L. and P.W.

Competing interests

The authors declare no competing interests.

Additional information

Extended data is available for this paper at https://doi.org/10.1038/s43018-025-01058-2.

Supplementary information The online version contains supplementary material available at https://doi.org/10.1038/s43018-025-01058-2.

Correspondence and requests for materials should be addressed to Ye Li or Peng Wang.

Peer review information *Nature Cancer* thanks Wei-Jun Fan, Flavio G. Rocha and the other, anonymous, reviewer(s) for their contribution to the peer review of this work.

[1]Department of Hepatobiliary Oncology, Zhongshan Hospital, Fudan University, Shanghai, China. [2]Liver Cancer Institute, Zhongshan Hospital; Key Laboratory of Carcinogenesis and Cancer Invasion (Ministry of Education), Fudan University, Shanghai, China. [3]National Clinical Research Center for Interventional Medicine, Shanghai, China. [4]Department of Integrative Oncology, Fudan University Shanghai Cancer Center, Shanghai, China. [5]Department of Biostatistics, Clinical Research Unit, Institute of Clinical Science, Zhongshan Hospital, Fudan University, Shanghai, China. [6]These authors contributed equally: Sijia Gu, Qiyu Luo. ✉e-mail: li_ye@fudan.edu.cn; peng_wang@fudan.edu.cn

https://doi.org/10.1038/s43018-025-01058-2

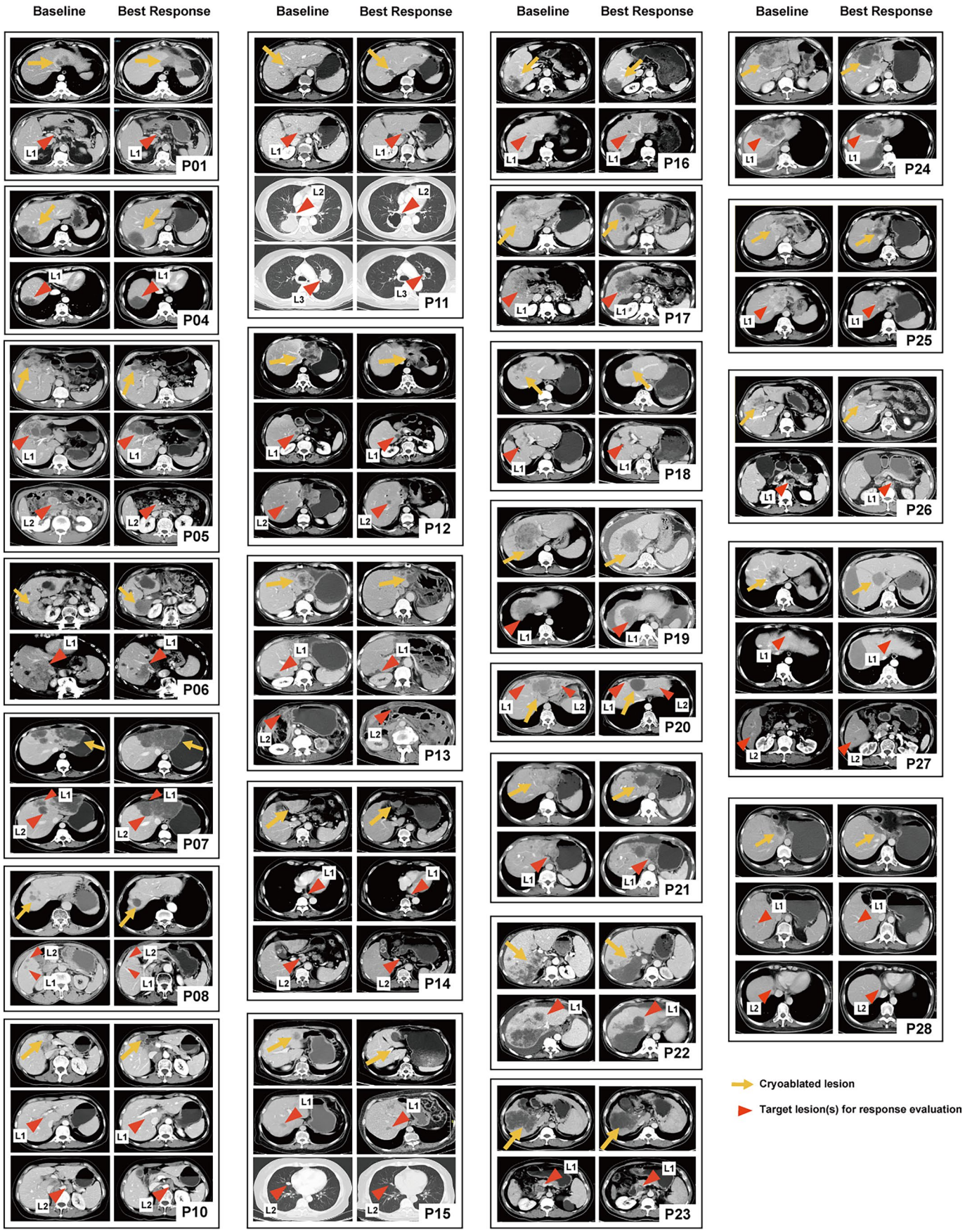

Extended Data Fig. 1 | Representative images for each patient. Representative images of 25 patients at baseline and at their best response.

https://doi.org/10.1038/s43018-025-01058-2

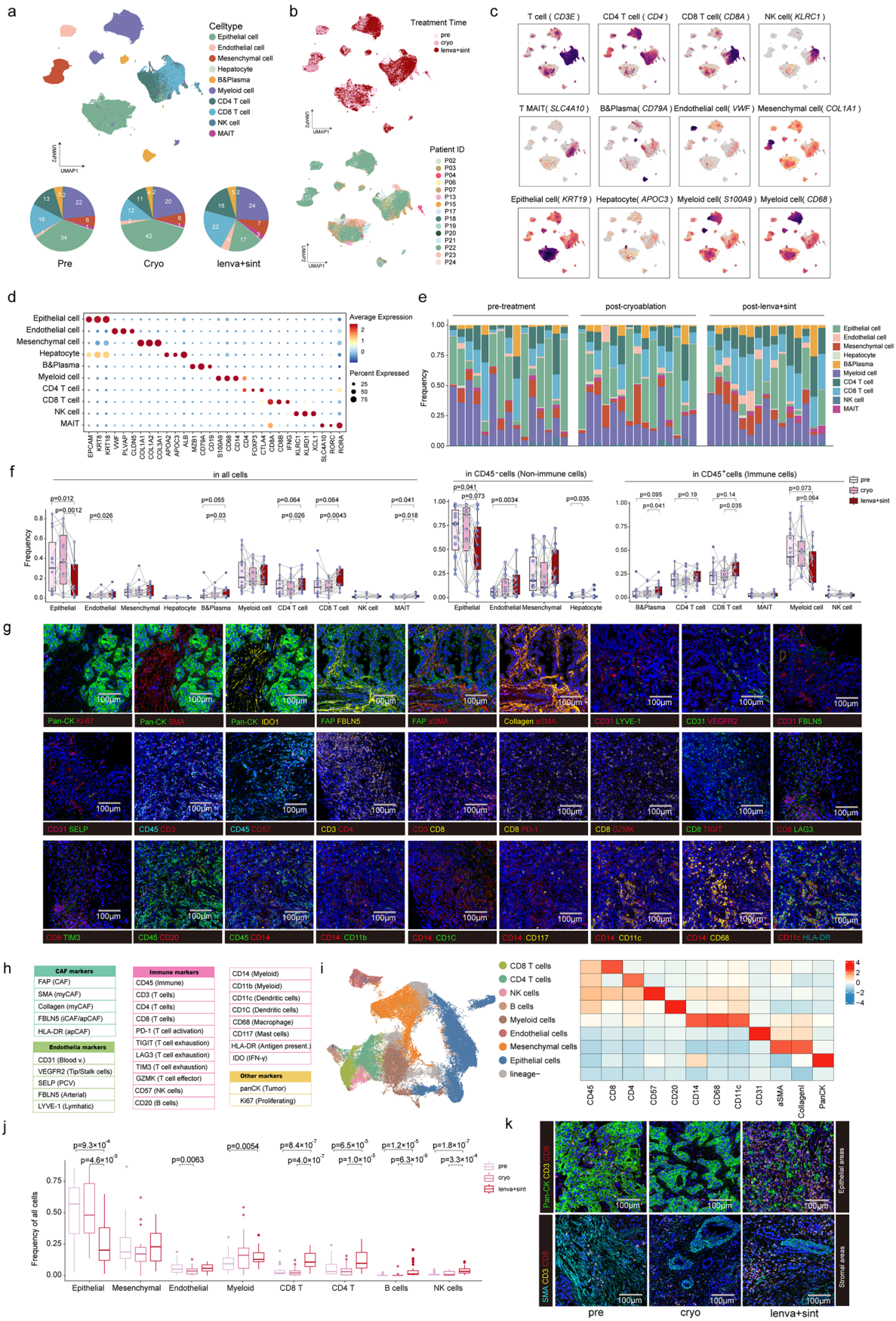

Extended Data Fig. 2 | See next page for caption.

https://doi.org/10.1038/s43018-025-01058-2

Extended Data Fig. 2 | Cellular overview of tumors before and after treatment. **a**, Uniform manifold approximation and projection (UMAP) embedding of 267,018 cells in 45 scRNA-seq samples, colored and labeled by cell type (upper panel). Pie plot showing percentage of ten major clusters stratified by three time points (lower panel). **b**, UMAP embedding of scRNA-seq data colored and labeled by treatment time (upper panel) and Patient ID (lower panel). **c**, **d**, Expression of marker genes for each major cell type identified in scRNA-seq data using UMAP embedding (**c**) and dot plot (**d**). In dot plot, dot size represents the percentage of cells in which the gene is detected. Color indicates the mean expression. **e**, Bar plot displaying the prevalence and proportion of the major subgroups of 45 scRNA-seq samples, stratified by three time points. **f**, Box plot of scRNA-seq data showing the dynamic changes in all cells(left), in $CD45^-$ non-immune cells (middle) and in $CD45^+$ immune cells (right) of paired samples stratified by three time points: pre-treatment (pre), post-cryoablation (post), and post levatinib-sintilimab (lenva+sint). Data analyzed by the two-sided paired Wilcoxon test. **g**, Representative images of all markers from 88 IMC ROIs of 5 patients. Scale bar, 100μm. **h**, Markers in the IMC antibody panel. **i**, Celltype annotation based on IMC markers. UMAP embedding of 89,924 cells, colored and labeled by major celltypes (left) and heatmap of average marker expression for cell phenotypes on population level (right). **j**, Box plot showing the dynamic changes of celltypes in all cells stratified by three time points (pre n=32, cryo n=27, lenva+sint n=29) in all cells in IMC data obtained from 5 patients. Data analyzed by the unpaired two-sided Wilcoxon test. **k**, Representative images showing the distribution of $CD8^+$ T cells in epithelial areas and stromal cells among three time points from 88 IMC ROIs of 5 patients. Scale bar, 100μm. For **a**-**f**, data was obtained from 45 scRNA-seq samples at three time points (each time point, n =15). For **f**, **j**, center line indicates the median value, bottom and top hinges represent the 25th and 75th percentiles, respectively and whiskers denote 1.5 × interquartile range.

https://doi.org/10.1038/s43018-025-01058-2

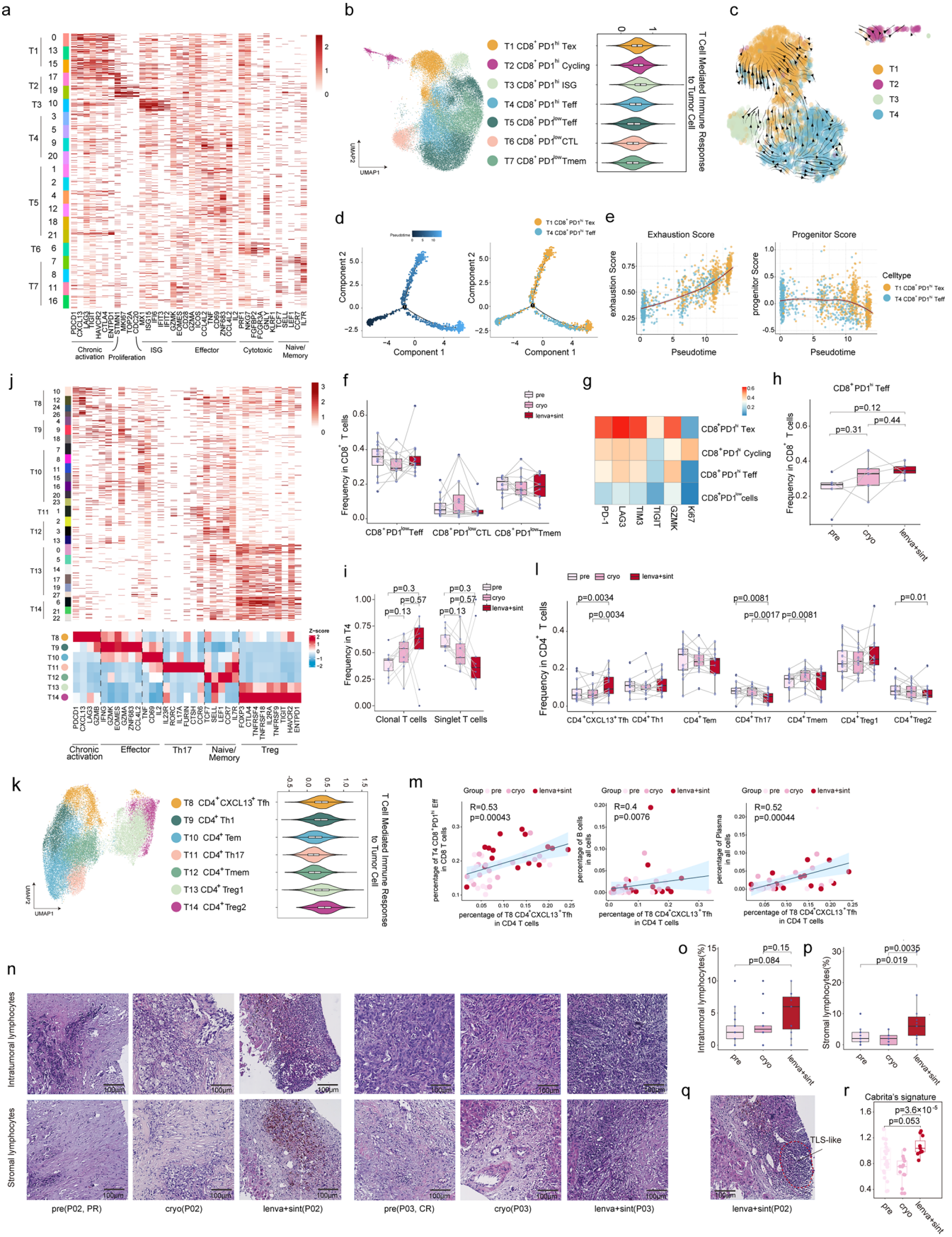

Extended Data Fig. 3 | See next page for caption.

https://doi.org/10.1038/s43018-025-01058-2

Extended Data Fig. 3 | Detailed characterization of CD8$^+$ and CD4$^+$ T cell subclusters. a, Heatmap showing expression of cluster-defining gene modules by CD8$^+$ T cells at single cell level in the scRNA-seq data. **b**, Sub-clustering of CD8$^+$ T cells, colored and labeled by subclusters (left) and corresponding Tumor-reactive T cell signature score of each subcluster (right). **c**, RNA velocities overlaid on the UMAP of CD8$^+$PD-1^{hi} T cells in the scRNA-seq data. The arrow represents a spatial trajectory. Dots are colored by CD8$^+$PD-1^{hi} T cell subclusters. **d**, Pseudotime-ordered analysis of T1 and T4 clusters inferred by Monocle2 in the scRNA-seq data. Dots are colored by Pseudotime (left) and celltype (right). **e**, Scatterplots showing exhaustion score (left) and progenitor score (right) of T1 and T4 along Pseudotime. **f**, Box plot of scRNA-seq data showing the dynamic proportional changes of CD8$^+$PD-1^{low} T-cell subtypes in CD8$^+$ T cells of paired samples stratified by three time points; each time point, *n*=12. **g**, Heatmap showing CD8$^+$ T celltype annotation based on average expression of cluster-defining gene expression at the population level in IMC data obtained from 5 patients. **h**, Box plot of IMC data showing the dynamic proportional changes of CD8$^+$PD-1^{hi} Teff in CD8$^+$ T cells of paired samples stratified by three time points; each time point, *n*=5. **i**, Box plot illustrating frequencies of clonal (left) and singlet (right) clones of CD8$^+$PD1^{hi}Teff stratified by three time points (each timepoint *n*=9) in scTCR data. **j**, Heatmap showing expression of cluster-defining gene modules by CD4$^+$ T cells at single cell level (upper panel) and standardized average expression of each subcluster at the population level (lower panel) in the scRNA-seq data. **k**, Sub-clustering of CD4$^+$ T cells, colored and labeled by subclusters (left) and corresponding Tumor-reactive T cell signature score of each subcluster (right). **l**, Box plot showing the dynamic proportional changes of CD4$^+$ T cell subtypes of paired samples at three time points; each time point *n*=13 in the scRNA-seq data. **m**, Scatterplots showing significant correlations in the scRNA-seq data between CD4$^+$CXCL13$^+$Tfh proportion in CD4$^+$ T cells with percentage of CD8$^+$PD-1^{hi} Teff in CD8$^+$ T cells(left); percentage of B cells in all cells(middle); and percentage of Plasma in all cells(right). Analyzed by two-sided Spearman correlation test, the shaded area indicates the 95% CI of the fit. **n**, Representative H&E-stained images depicting intratumoral and stromal lymphocytes from P02 (left), who achieved partial response (PR); and P03 (right), who achieved complete response (CR), at three distinct time points. Scale bar, 100μm. **o**, **p**, Boxplots showing the dynamic changes in intratumoral (**o**) and stromal (**p**) lymphocyte densities identified in H&E-stained images at three time points; pre *n*=21, cryo *n*=16, lenva+sint *n*=11. **q**, Representative image of a tertiary lymphoid structure (TLS)-like formation observed in P02 following lenva+sint. Scale bar, 100μm. **r**, Box plot displaying the Cabrita's signature score in bulk RNA-seq samples among three time points; pre *n*=22, cryo *n*=13, lenva+sint *n*=11. For **a-e, j, k, m**, data was obtained from 45 scRNA-seq samples at three time points (each time point, *n* =15). For **b, f, h, i, k, l, o, p, r**, center line indicates the median value, bottom and top hinges represent the 25th and 75th percentiles, respectively and whiskers denote 1.5 × interquartile range. For **f, h, i, l**, paired two-sided Wilcoxon test was applied. For **o, p, r**, unpaired two-sided Wilcoxon test was applied. For **n, q**, representative images from 48 H&E-stained images of 20 patients.

https://doi.org/10.1038/s43018-025-01058-2

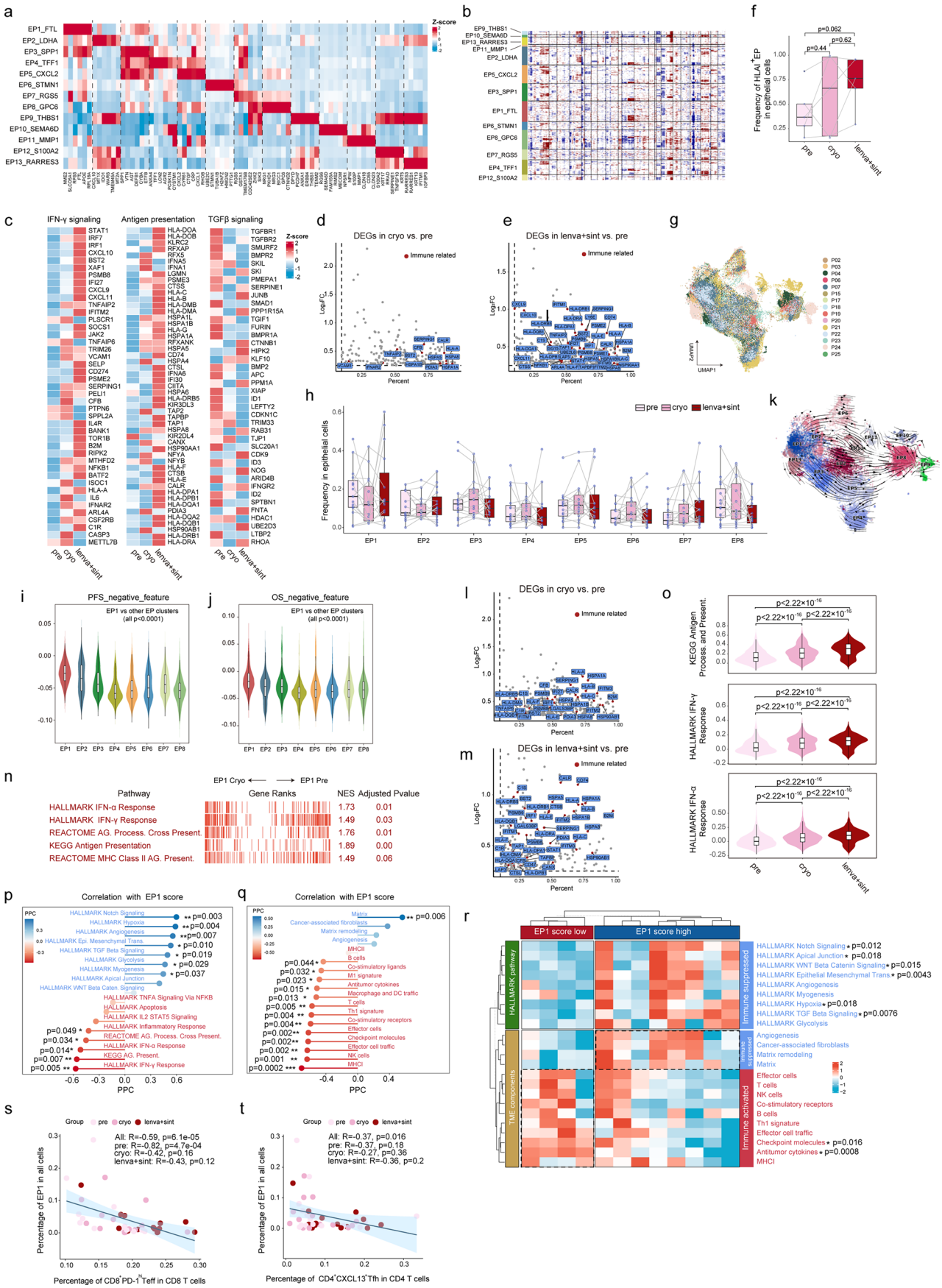

Extended Data Fig. 4 | See next page for caption.

https://doi.org/10.1038/s43018-025-01058-2

Extended Data Fig. 4 | Features of malignant cell clusters, especially EP1 during treatment process. a, Heatmap showing standardized average expression values of cluster-defining genes in epithelial (EP) cell clusters in the scRNA-seq data on population level. **b**, Copy number variation (CNV) profile using InferCNV based on single-cell EP cells. **c**, Heatmap displaying dynamic changes of typical genes of immune-related modules in all EP cells in the scRNA-seq data on population level at three time points. **d**,**e**, Volcano plots showing the DEGs in all EP cells, including (**d**) post-cryoablation versus pre-treatment and (**e**) post lenva+sint versus pre-treatment(each time point n =15). The x axis and y axis values were calculated by the Seurat method. All points indicate significantly upregulated genes (P<0.05). Immune-related DEGs are labeled. **f**, Box plot of IMC data showing the dynamic proportional changes of $HLAI^{+}$EPs in all EP cells of paired samples stratified by three time points; each time point n=5; paired two-sided Wilcoxon test. **g**, Sub-clustering of EP cells in the scRNA-seq data, colored and labeled by patients. **h**, Box plot of scRNA-seq data showing the dynamic changes in EP subtypes of paired samples stratified by three time points. **i**, **j**, Violin plot showing the quantification of PFS negative signature scores (left) and OS negative signature scores (right) in EP cells among various EP subgroups. Analyzed by One-way ANOVA test. **k**, RNA velocities overlaid on the UMAP of EP cells in the scRNA-seq data. The arrow represents a spatial trajectory. Dots are colored by EP subclusters. **l**, **m**, Volcano plots showing the DEGs in EP1 in the scRNA-seq data, including (**l**) post-cryoablation versus pre-treatment and (**m**) post lenva+sint versus pre-treatment(each time point, n =15). The x axis and y axis values were calculated by the Seurat method. All points indicate significantly upregulated genes (P<0.05). Immune-related DEGs are labeled. **n**, GSEA enrichment for gene sets in EP1 cells after cryoablation comparing with before treatment (each time point, n =15). P values were determined by one-tailed permutation test by GSEA. **o**, Violin plots showing the signature scores of signatures (KEGG antigen processing and presenting, Hallmark IFNγ response and IFNα response) of EP1 cells at three time points. Two-sided Wilcoxon test. **p**, **q**, Correlations of EP1 signature score with Hallmark pathway scores (**p**) and immune components scores (**q**) in 22 bulk RNA-seq samples at baseline. PCC, Pearson correlation coefficient. *p < 0.05, **p < 0.01, ***p < 0.001. **r**, Heatmap showing abundance of pathways and TME components in 12 post-cryoablation bulk RNA-seq samples stratified by median baseline EP1 signature scores into high- and low-EP1 signature groups. *Significantly differentially expressed pathways (two-sided t-test, *p<0.05). **s**,**t**, Scatterplots showing significant correlations in the scRNA-seq data between EP1 cellular proportion in all cells with percentage of CD8+PD-1^{hi} Teff in $CD8^{+}$ T cells (**s**) and percentage of $CD4^{+}CXCL13^{+}$Tfh in $CD4^{+}$ T cells (**t**). Two-sided Spearman correlation test, the shaded area indicates the 95% CI of the fit. For **a-c, g-k o, s, t**, data was obtained from 45 scRNA-seq samples at three time points (each time point, n =15). For **f, h, i, j, o**, center line indicates the median value, bottom and top hinges represent the 25th and 75th percentiles, respectively and whiskers denote 1.5 × interquartile range.

https://doi.org/10.1038/s43018-025-01058-2

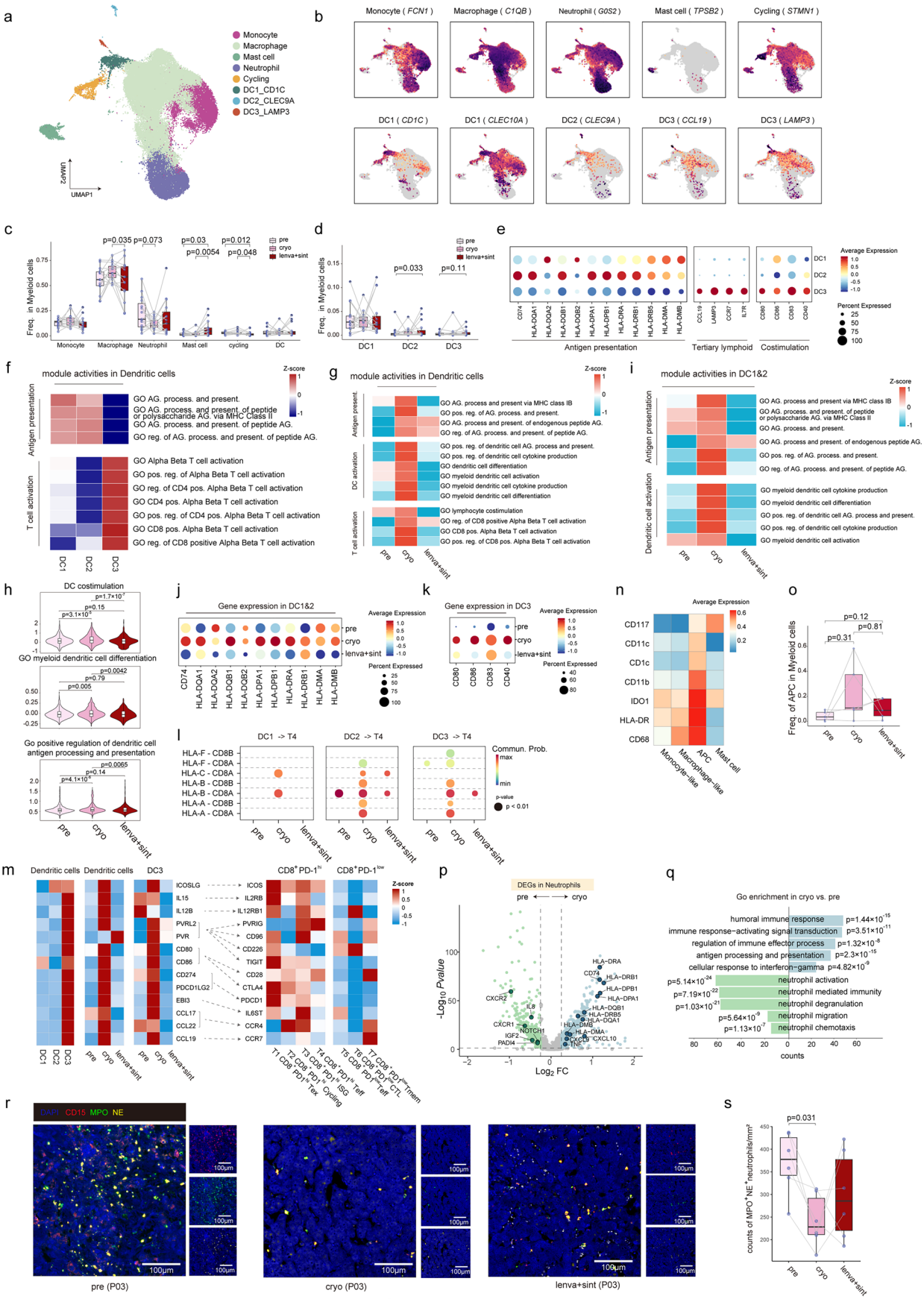

Extended Data Fig. 5 | See next page for caption.

https://doi.org/10.1038/s43018-025-01058-2

Extended Data Fig. 5 | Features of dendritic cell clusters across treatment process. a, Sub-clustering of myeloid cells colored and labeled by subclusters. **b**, UMAP embeddings showing the expression of selected marker genes in myeloid cells. **c**,**d**, Box plot showing the dynamic proportional changes in myeloid cell subtypes (**c**) and DC subtypes (**d**) of paired samples stratified by three time points. **e**, Dot plots showing the expression level of selected genes in dendritic cell (DC) subclusters of scRNA-seq data. Dot size represents the percentage of cells in which the gene is detected. Color indicates the mean expression. **f**,**g**,**i**, Heatmap showing scaled mean activities of selected modules in DC subgroups (**f**), among three time points in all DCs (**g**) and among three time points in DC1 and DC2 (**i**) at population level. **h**, Violin plots showing scores of DC-related signatures in all DCs at three time points. **j**,**k**, Dot plots showing the expression levels of selected genes in DC1 and DC2 (**j**), and DC3 (**k**) of scRNA-seq data at the three time points. Dot size indicates the percentage of cells in which the gene was detected. Color indicates the mean expression. **l**, Receptor–ligand pairs of DC subclusters with $CD8^+PD\text{-}1^{hi}$ Teffs inferred by scRNA-seq data with significant differences between the three time points. The larger dot size indicates a significant P value. Colors illustrate the communication probability of the indicated pathways. **m**, Ligand-receptor pair expression analysis between DC subgroups and $CD8^+$ T cell subgroups of scRNA-seq data, with heatmap showing average gene expression on population level. **n**, Heatmap showing myeloid celltype annotation based on average cluster-defining gene expression at population level in IMC data from 5 patients. **o**, Box plot of IMC data showing the dynamic proportional changes of $IDO1^+$ $HLA\text{-}DR^+$APCs in myeloid cells of paired samples stratified by three time points; each time point, n=5. **p**, Volcano plots showing the DEGs in neutrophils post-cryoablation versus pre-treatment of scRNA-seq data (each time point, n =15). The x axis and y axis values were calculated by the Seurat method. Green points indicate upregulated genes pre-treatment, and blue points indicate upregulated genes post-cryoablation. Representative significant DEGs of interest are labeled. **q**, Comparative gene set enrichment analysis of pre-treatment and post cryoablation gene sets in the neutrophils of scRNA-seq (each time point, n =15). P values determined by two-sided Fisher exact test. **r**, Representative multiplex immunofluorescence (mIF) images showing the distributions of $CD15^+MPO^+NE^+$ neutrophils patient P03 at the three time points. Scale bars: 100 μm. **s**, Quantitative analysis of mIF data revealing the dynamic changes in $CD15^+MPO^+NE^+$ neutrophils stratified by the three time points; each time point n=6. For **a**-**m**, data was obtained from 45 scRNA-seq samples at three time points (each time point, n =15). For **c, d, h, o, s**, center line indicates the median value, bottom and top hinges represent the 25th and 75th percentiles, respectively and whiskers denote 1.5 × interquartile range; For **c, d, o, s**, paired two-sided Wilcoxon test was applied. For **h, p**, unpaired two-sided Wilcoxon test was applied.

https://doi.org/10.1038/s43018-025-01058-2

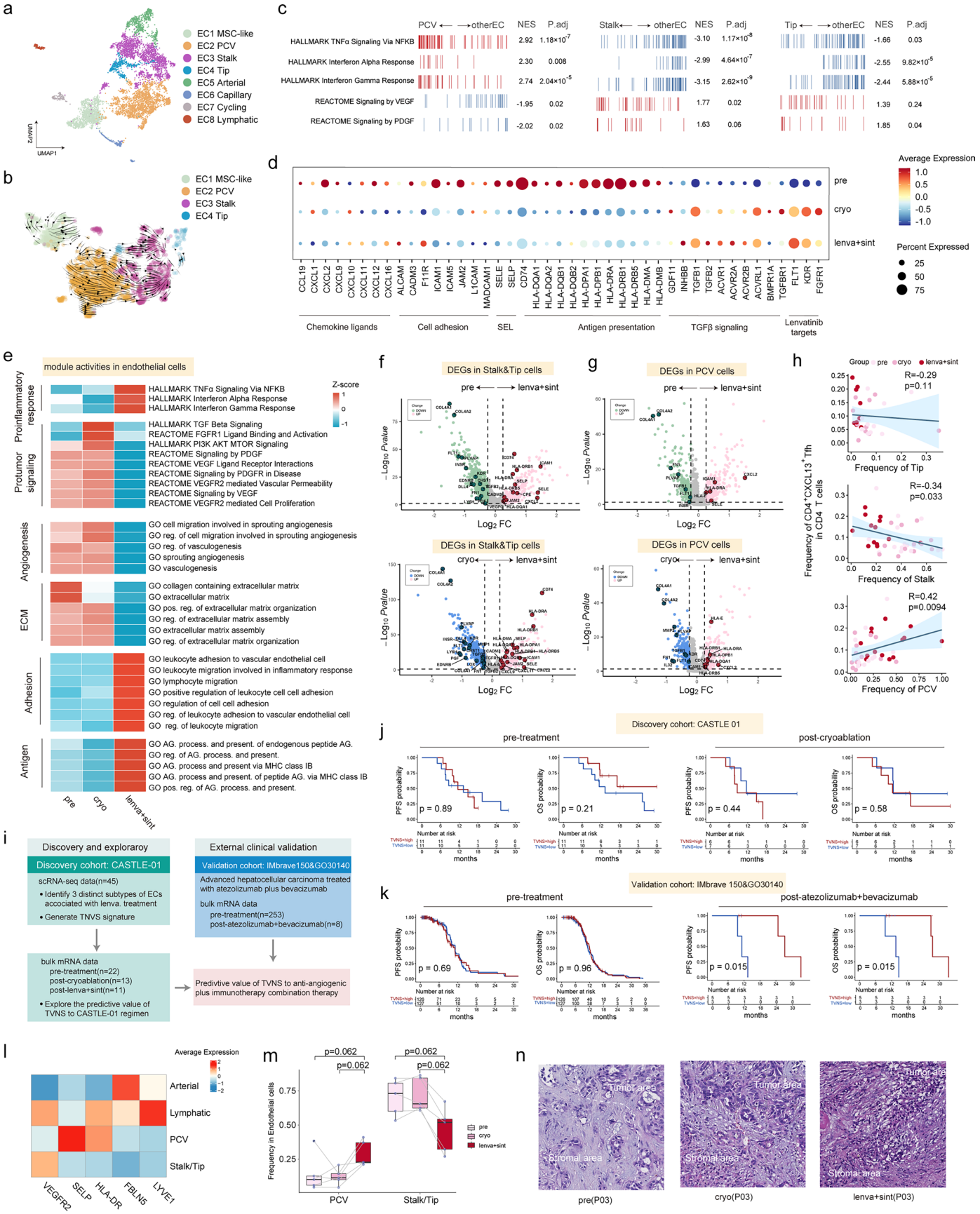

Extended Data Fig. 6 | See next page for caption.

https://doi.org/10.1038/s43018-025-01058-2

Extended Data Fig. 6 | Features of endothelial cell clusters during treatment process. a, Sub-clustering of endothelial cells (ECs) of scRNA-seq data, colored and labeled by subclusters. **b**, RNA velocities overlaid on the UMAP of EC subtypes of scRNA-seq data. The arrow represents a spatial trajectory. Dots are colored by EC subclusters. **c**, GSEA enrichment for gene sets in PCV cells(left), stalk cells(middle), tip cells(right) compared with other EC cells respectively of scRNA-seq data. NES, normalized enrichment score. P values were determined by one-tailed permutation test by GSEA. **d**,**e**, Dynamic changes in transcriptional characteristics of all ECs of scRNA-seq data at the three time points, as illustrated by a dot plot showing the expression levels of selected genes (**d**) and a heatmap showing scaled mean activities of selected modules at population level (**e**). Dot size represents the percentage of cells in which the gene was detected. Color indicates the mean expression. **f**,**g**, Volcano plots showing the DEGs in stalk and tip cells (**f**) and PCV cells (**g**) of scRNA-seq data, including post lenva+sint versus pre-treatment (upper panel) and post lenva+sint versus post-cryoablation (lower panel) (each time point, n =15). The x axis and y axis values were calculated by the Seurat method, two-sided unpaired Wilcoxon test was applied. Green points indicate upregulated genes pre-treatment, blue points indicate upregulated genes post-cryoablation and red points indicate upregulated genes post lenva+sint. Representative significant DEGs of interest are labeled. **h**, Scatterplots showing significant correlations between $CD4^+CXCL13^+$Tfh proportion in $CD4^+$T cells with percentage of tip cells (upper panel), stalk cells (middle panel) and PCV cells (lower panel) in all ECs of scRNA-seq data. Two-sided Spearman correlation test, the shaded area indicates the 95% CI of the fit. **i**, Flow chart of biospecimen inclusions for the exploration of TVNS in discovery cohort (left) and external clinical validation (upper-right). **j**, Kaplan–Meier survival curves for PFS and OS, grouped by high and low TVNSs of pre-treatment(left, n=22) and post-cryoablation (right, n=13) bulk RNA-seq samples from the CASTLE-01 discovery cohort, analyzed by the log-rank test. **k**, Kaplan–Meier survival curves for PFS and OS, grouped by high and low TVNSs of pre-treatment (left, n=253) and post atezolizumab+bevacizumab (right, n=8) bulk RNA-seq samples from the IMbrave 150 and GO30140 validation cohort, analyzed by the log-rank test. **l**, Heatmap showing EC celltype annotation based on cluster-defining average gene expression in IMC data obtained from 5 patients at population level. **m**, Box plot of IMC data showing the dynamic proportional changes of PCV, Stalk-Tip clusters in ECs of paired samples stratified by three time points; each time point, n=5; center line indicates the median value, bottom and top hinges represent the 25th and 75th percentiles, respectively and whiskers denote 1.5 × interquartile range; two-sided paired Wilcoxon test. **n**, Stromal area and tumor area division based on H&E staining in P03 ROIs from 5 patients included in IMC analysis. For **a-e, h**, data was obtained from 45 scRNA-seq samples at three time points (each time point, n =15).

https://doi.org/10.1038/s43018-025-01058-2

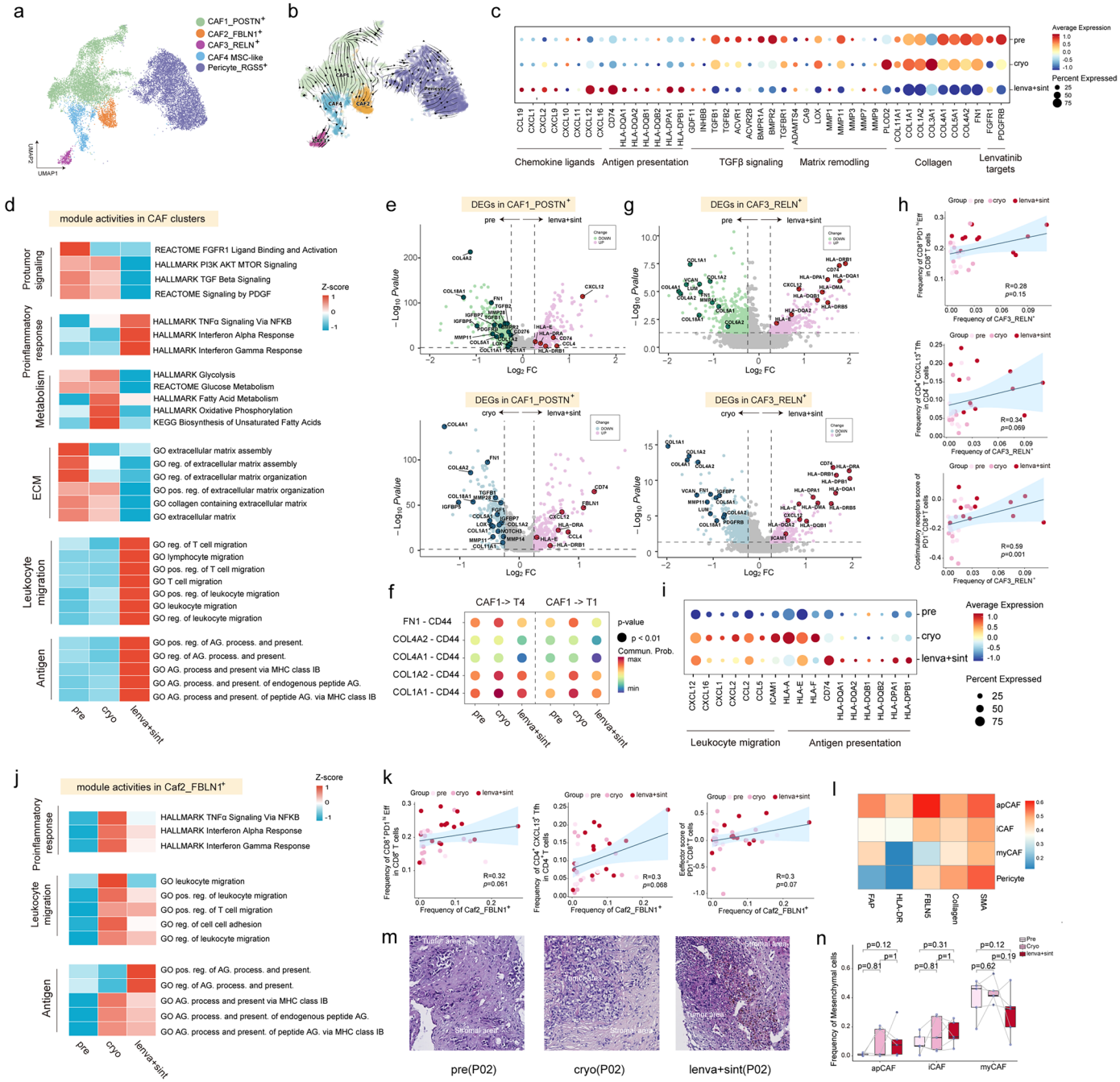

Extended Data Fig. 7 | See next page for caption.

https://doi.org/10.1038/s43018-025-01058-2

Extended Data Fig. 7 | Description of cancer associated fibroblast subclusters across treatment process. a, Sub-clustering of mesenchymal cell clusters of scRNA-seq data colored and labeled by subclusters. **b**, RNA velocities overlaid on the UMAP of mesenchymal subtypes of scRNA-seq data. The arrow represents a spatial trajectory. Dots are colored by mesenchymal cell subclusters. **c**,**d**, Dynamic changes in transcriptional characteristics of all CAF cells of scRNA-seq at the three time points, as illustrated by a dot plot showing the expression levels of selected genes (**c**) and a heatmap showing scaled average activities selected modules at population level (**d**). Dot size indicates the percentage of cells in which the gene was detected. Color indicates the mean expression. **e**, **g**, Volcano plots showing the DEGs in CAF1(**e**) and CAF3(**g**) of scRNA-seq data, including post lenva+sint versus pre-treatment (upper panel) and post lenva+sint versus post-cryoablation (lower panel)(each time point, n =15). The x axis and y axis values were calculated by the Seurat method, two-sided unpaired Wilcoxon test was applied. Green points indicate upregulated genes pre-treatment, blue points indicate upregulated genes post-cryoablation and red points indicate upregulated genes post lenva+sint. Representative significant DEGs of interest are labeled. **f**, Receptor–ligand pairs that differ significantly between three time points based on CAF1 with $CD8^+PD\text{-}1^{hi}$ Tex and $CD8^+PD\text{-}1^{hi}$ Teff of scRNA-seq data. Dot size implies p value, colored based on the communication probability of pathways. **h**, Scatterplots showing significant correlations in scRNA-seq data between the percentage of CAF3 in mesenchymal cells with $CD8^+PD\text{-}1^{hi}$ Teff proportion in $CD8^+$ T cells (upper panel), $CD4^+CXCL13^+$Tfh proportion in $CD4^+$ T cells (middle panel) and costimulatory score in $CD8^+PD\text{-}1^{hi}$ T cells (lower panel). Two sided spearman correlation test. **i**,**j**, Dynamic changes in transcriptional characteristics of CAF2 cells of scRNA-seq data at the three time points, as illustrated by a dot plot showing the expression levels of selected genes (**i**) and a heatmap showing scaled average activities selected modules at population level (**j**). Dot size indicates the percentage of cells in which the gene was detected. Color indicates the mean expression. **k**, Scatterplots showing significant correlations of scRNA-seq data between the percentage of CAF2 in mesenchymal cells with $CD8^+PD\text{-}1^{hi}$ Teff proportion in $CD8^+$ T cells (left), $CD4^+CXCL13^+$Tfh proportion in $CD4^+$ T cells (middle) and effector score in $CD8^+PD\text{-}1^{hi}$ T cells (right). Two sided spearman correlation test. **l**, Heatmap showing mesenchymal celltype annotation based on cluster-defining average gene expression at population level in IMC data obtained from 5 patients. **m**, Stromal area and tumor area division based on H&E staining in P02 ROIs from 5 patients included in IMC analysis. **n**, Box plot of IMC data showing the dynamic proportional changes of three CAF clusters in mesenchymal cells of paired samples stratified by three time points; each time point, n=5; center line indicates the median value, bottom and top hinges represent the 25th and 75th percentiles, respectively and whiskers denote 1.5 × interquartile range; two-sided paired Wilcoxon test. For **a-d, f, h-k**, data was obtained from 45 scRNA-seq samples at three time points (each time point, n =15). For **h, k**, the shaded area indicates the 95% CI of the fit.

nature portfolio

Corresponding author(s): Peng Wang

Last updated by author(s): Sep 6, 2025

Reporting Summary

Nature Portfolio wishes to improve the reproducibility of the work that we publish. This form provides structure for consistency and transparency in reporting. For further information on Nature Portfolio policies, see our Editorial Policies and the Editorial Policy Checklist.

Statistics

For all statistical analyses, confirm that the following items are present in the figure legend, table legend, main text, or Methods section.

n/a	Confirmed
☐	☒ The exact sample size (*n*) for each experimental group/condition, given as a discrete number and unit of measurement
☐	☒ A statement on whether measurements were taken from distinct samples or whether the same sample was measured repeatedly
☐	☒ The statistical test(s) used AND whether they are one- or two-sided *Only common tests should be described solely by name; describe more complex techniques in the Methods section.*
☒	☐ A description of all covariates tested
☐	☒ A description of any assumptions or corrections, such as tests of normality and adjustment for multiple comparisons
☐	☒ A full description of the statistical parameters including central tendency (e.g. means) or other basic estimates (e.g. regression coefficient) AND variation (e.g. standard deviation) or associated estimates of uncertainty (e.g. confidence intervals)
☐	☒ For null hypothesis testing, the test statistic (e.g. *F*, *t*, *r*) with confidence intervals, effect sizes, degrees of freedom and *P* value noted *Give P values as exact values whenever suitable.*
☒	☐ For Bayesian analysis, information on the choice of priors and Markov chain Monte Carlo settings
☐	☒ For hierarchical and complex designs, identification of the appropriate level for tests and full reporting of outcomes
☐	☒ Estimates of effect sizes (e.g. Cohen's *d*, Pearson's *r*), indicating how they were calculated

Our web collection on statistics for biologists contains articles on many of the points above.

Software and code

Policy information about availability of computer code

Data collection	CYTOF Software v7.0 (Fluidigm) was used for running of the Hyperion imaging mass cytometry system and acquisition of samples. CellProfiler v4.0.6 (https://cellprofiler.org/) was used to generate mask files.
Data analysis	Data analysis in the present study was performed in R software (open source, v4.3.0). No new algorithms were developed for this study. All code generated for analysis is publicly available at Github (https://github.com/SJ-GU/CASTLE-01).

For manuscripts utilizing custom algorithms or software that are central to the research but not yet described in published literature, software must be made available to editors and reviewers. We strongly encourage code deposition in a community repository (e.g. GitHub). See the Nature Portfolio guidelines for submitting code & software for further information.

Data

Policy information about availability of data

All manuscripts must include a data availability statement. This statement should provide the following information, where applicable:

- Accession codes, unique identifiers, or web links for publicly available datasets
- A description of any restrictions on data availability
- For clinical datasets or third party data, please ensure that the statement adheres to our policy

The study protocol is available in the Supplementary Information file. De-identified individual participant data reported in the paper will be shared under data use agreements upon reasonable request. The sequencing data generated in this study (scRNA/TCR-seq, WES, bulk RNA-seq and bulk TCR seq

data) have been deposited into the Genome Sequence Archive (GSA) in the National Genomics Data Center, China National Center for Bioinformation/Beijing Institute of Genomics, Chinese Academy of Sciences (https://ngdc.cncb.ac.cn/gsa/), under project accession number (PRJCA025263, PRJCA025324, PRJCA025505, PRJCA025506). All sequencing data generated in this study are available under the terms of a Data Use Agreement that addresses the privacy and security requirements for safeguarding the data, and may only be used for research purposes. Response to access requests is typically expected within two weeks, and data will remain available to approved requesters for one month. For detailed instructions on how to request access, please refer to the GSA's guidelines. Previously published bulk RNA-seq data of IMbrave150 and GO30140 cohorts (accession codes: EGAC00001002314) are available upon request via the European Genome-phenome Archive at https://ega-archive.org/dacs/EGAC00001002314. The remaining data are available within the Article, its Supplementary Information and Source Data file and/or from the corresponding author on request. Source data are provided with this paper.

Research involving human participants, their data, or biological material

Policy information about studies with human participants or human data. See also policy information about sex, gender (identity/presentation), and sexual orientation and race, ethnicity and racism.

Reporting on sex and gender	Patients were recruited into the clinical trial regardless of gender. All patients whom are deemed to be candidates fit inclusion/exclusion criteria were offered participation in the clinical trial. The disaggregated sex data has been provided in Supplementary table 2 and consent has been obtained for sharing of individual-level data. 11 females and 17 males have been recruited in our study.
Reporting on race, ethnicity, or other socially relevant groupings	No socially constructed or socially relevant categorization variables was used in our manuscript.
Population characteristics	Eligible patients were 18 years older with histologically confirmed ICC before enrollment. Other eligibility criteria included the following: Eastern Cooperative Oncology Group (ECOG) performance status score 0–2; disease that was not amenable to potentially curative liver transplantation or resection; progression of disease on at least one line of chemotherapy, including GemCis; adequate organ and marrow function; and no history of chronic autoimmunity or inflammatory bowel disease. All enrolled patients had to have at least two distinct lesions, with one intrahepatic lesion amenable to cryoablation and the remaining lesion(s), either intrahepatic or extrahepatic, designated as the target lesion(s) for response assessment. More information of patients is available in Supplementary table 2.
Recruitment	All eligible patients had been histologically diagnosed with locally advanced or metastatic ICC and had radiological evidence of progressive disease at enrollment. A total of 36 patients were screened, and 6 of them were ineligible for inclusion: 3 with inadequate organ function, 2 with exclusionary previous immunotherapy/target therapy and 1 with no lesion for response evaluation apart from ablated lesion. With 2 additional patients withdrawing their consent, 28 patients were recruited eventually, from first patient on August 24, 2021, to the last patient on May 12, 2023.
Ethics oversight	The study protocol and amendments were approved by the ethics committee of the Fudan University Shanghai Cancer Center, Shanghai (Approval No. 1905201-11). The trial was performed in accordance with the principles of Good Clinical Practice and the Declaration of Helsinki. All patients provided written, informed consent for participation and publication of potentially identifying clinical information prior to enrollment. The ClinicalTrials.gov identifier is NCT05010668 (https://clinicaltrials.gov/study/NCT05010668) (preregistered at August 11, 2021).The study protocol is included in the Supplementary Information.

Note that full information on the approval of the study protocol must also be provided in the manuscript.

Field-specific reporting

Please select the one below that is the best fit for your research. If you are not sure, read the appropriate sections before making your selection.

☒ Life sciences ☐ Behavioural & social sciences ☐ Ecological, evolutionary & environmental sciences

For a reference copy of the document with all sections, see nature.com/documents/nr-reporting-summary-flat.pdf

Life sciences study design

All studies must disclose on these points even when the disclosure is negative.

Sample size	Sample size was calculated using a binomial exact single-stage phase 2 design. Considering that the ORR of the standard second-line treatment regimen FOLFOX is 5%, and the phase 2 study of lenvatinib plus pembrolizumab reported an ORR of 10%, the null hypothesis was that an ORR rate of 10% cryoablation followed by lenvatinib-sintilimab would not be worthy of further evaluation in this population. The alternative hypothesis was that an ORR rate of 30% for the combination of cryoablation followed by lenvatinib-sintilimab would be promising, with 25 patients providing > 80% power to detect this increase in ORR at a two-sided 5% significance level.
Data exclusions	No data were excluded in the analysis.
Replication	We used different analytical methods to verify the reproducibility of the experimental findings wherever possible and all attempts at replication were successful.
Randomization	This is a proof of concept sing-arm phase 2 clinical trial with one treatment regimen, so this is no randomization.Mouse tumor experiments were randomized so that the groups had no differences in mean body weight at the start of the experiment.

Blinding	This is a proof of concept sing-arm phase 2 clinical trial with one treatment regimen, so there is no need to blinding.Flow cytometry experiments and pathology assessment were conducted in a blinded fashion, whereas other experiments were not, as the experiments were conducted and analyzed by the same researchers.

Behavioural & social sciences study design

All studies must disclose on these points even when the disclosure is negative.

Study description	*Briefly describe the study type including whether data are quantitative, qualitative, or mixed-methods (e.g. qualitative cross-sectional, quantitative experimental, mixed-methods case study).*
Research sample	*State the research sample (e.g. Harvard university undergraduates, villagers in rural India) and provide relevant demographic information (e.g. age, sex) and indicate whether the sample is representative. Provide a rationale for the study sample chosen. For studies involving existing datasets, please describe the dataset and source.*
Sampling strategy	*Describe the sampling procedure (e.g. random, snowball, stratified, convenience). Describe the statistical methods that were used to predetermine sample size OR if no sample-size calculation was performed, describe how sample sizes were chosen and provide a rationale for why these sample sizes are sufficient. For qualitative data, please indicate whether data saturation was considered, and what criteria were used to decide that no further sampling was needed.*
Data collection	*Provide details about the data collection procedure, including the instruments or devices used to record the data (e.g. pen and paper, computer, eye tracker, video or audio equipment) whether anyone was present besides the participant(s) and the researcher, and whether the researcher was blind to experimental condition and/or the study hypothesis during data collection.*
Timing	*Indicate the start and stop dates of data collection. If there is a gap between collection periods, state the dates for each sample cohort.*
Data exclusions	*If no data were excluded from the analyses, state so OR if data were excluded, provide the exact number of exclusions and the rationale behind them, indicating whether exclusion criteria were pre-established.*
Non-participation	*State how many participants dropped out/declined participation and the reason(s) given OR provide response rate OR state that no participants dropped out/declined participation.*
Randomization	*If participants were not allocated into experimental groups, state so OR describe how participants were allocated to groups, and if allocation was not random, describe how covariates were controlled.*

Ecological, evolutionary & environmental sciences study design

All studies must disclose on these points even when the disclosure is negative.

Study description	*Briefly describe the study. For quantitative data include treatment factors and interactions, design structure (e.g. factorial, nested, hierarchical), nature and number of experimental units and replicates.*
Research sample	*Describe the research sample (e.g. a group of tagged Passer domesticus, all Stenocereus thurberi within Organ Pipe Cactus National Monument), and provide a rationale for the sample choice. When relevant, describe the organism taxa, source, sex, age range and any manipulations. State what population the sample is meant to represent when applicable. For studies involving existing datasets, describe the data and its source.*
Sampling strategy	*Note the sampling procedure. Describe the statistical methods that were used to predetermine sample size OR if no sample-size calculation was performed, describe how sample sizes were chosen and provide a rationale for why these sample sizes are sufficient.*
Data collection	*Describe the data collection procedure, including who recorded the data and how.*
Timing and spatial scale	*Indicate the start and stop dates of data collection, noting the frequency and periodicity of sampling and providing a rationale for these choices. If there is a gap between collection periods, state the dates for each sample cohort. Specify the spatial scale from which the data are taken*
Data exclusions	*If no data were excluded from the analyses, state so OR if data were excluded, describe the exclusions and the rationale behind them, indicating whether exclusion criteria were pre-established.*
Reproducibility	*Describe the measures taken to verify the reproducibility of experimental findings. For each experiment, note whether any attempts to repeat the experiment failed OR state that all attempts to repeat the experiment were successful.*
Randomization	*Describe how samples/organisms/participants were allocated into groups. If allocation was not random, describe how covariates were controlled. If this is not relevant to your study, explain why.*
Blinding	*Describe the extent of blinding used during data acquisition and analysis. If blinding was not possible, describe why OR explain why blinding was not relevant to your study.*

Did the study involve field work? ☐ Yes ☐ No

Field work, collection and transport

Field conditions	*Describe the study conditions for field work, providing relevant parameters (e.g. temperature, rainfall).*
Location	*State the location of the sampling or experiment, providing relevant parameters (e.g. latitude and longitude, elevation, water depth).*
Access & import/export	*Describe the efforts you have made to access habitats and to collect and import/export your samples in a responsible manner and in compliance with local, national and international laws, noting any permits that were obtained (give the name of the issuing authority, the date of issue, and any identifying information).*
Disturbance	*Describe any disturbance caused by the study and how it was minimized.*

Reporting for specific materials, systems and methods

We require information from authors about some types of materials, experimental systems and methods used in many studies. Here, indicate whether each material, system or method listed is relevant to your study. If you are not sure if a list item applies to your research, read the appropriate section before selecting a response.

Materials & experimental systems

n/a	Involved in the study
☐	☒ Antibodies
☐	☒ Eukaryotic cell lines
☒	☐ Palaeontology and archaeology
☐	☒ Animals and other organisms
☐	☒ Clinical data
☒	☐ Dual use research of concern
☒	☐ Plants

Methods

n/a	Involved in the study
☒	☐ ChIP-seq
☐	☒ Flow cytometry
☒	☐ MRI-based neuroimaging

Antibodies

Antibodies used

Antibodies for imaging mass cytometry
Anti-human HLAI Abcam Cat# ab239788; RRID: AB_3665873 1:200
Anti-human CD14 Abcam Cat# ab226121 1:200
Anti-human FBLN5 Abcam Cat# ab66339; RRID: AB_2231921 1:50
Anti-human CD4 Abcam Cat# ab181724; RRID: AB_2864377 1:200
Anti-human CD8a Biolegend Cat# 372902; RRID: AB_2650657 1:100
Anti-human CollagenI Abcam Cat# ab215969; RRID: AB_2909621 1:200
Anti-human CD31 CST Cat# 85873SF 1:200
Anti-human TIM3 Abcam Cat# ab242080 1:150
Anti-human CD45 CST Cat# 47937SF 1:50
Anti-human TIGIT Abcam Cat# ab243903; RRID: AB_2943164 1:200
Anti-human IDO-1 Proteintech Cat# 66528-1-Ig; RRID: AB_2881891 1:200
Anti-human LAG-3 Abcam Cat# ab241407 1:50
Anti-human CD68 Biolegend Cat# 916104; RRID: AB_2616797 1:500
Anti-human CD11b Abcam Cat# ab209970; RRID: AB_2915959 1:200
Anti-human CD20 Abcam Cat# ab213033 1:100
Anti-human CD11c Abcam Cat# ab216655; RRID: AB_2864379 1:150
Anti-human GZMK Abcam Cat# ab282714; RRID: AB_3665531 1:50
Anti-human PD-1 CST Cat# 63815SF; RRID: AB_3675993 1:50
Anti-human Ki-67 BD Cat# 550609; RRID: AB_393778 1:300
Anti-human CD1C Abcam Cat# ab270797; RRID: AB_2884015 1:100
Anti-human HLA-DR NOVUS Cat# NB600-989 1:500
Anti-human CD117 Abcam Cat# ab216450; RRID: AB_2868615 1:200
Anti-human CD3 CST Cat# 24581SF 1:50
Anti-human FAP Abcam Cat# ab271976 1:50
Anti-human VEGFR2 Abcam Cat# ab315239 1:50
Anti-human CD57 BD Cat# 555618; RRID: AB_395985 1:600
Anti-human SELP Abcam Cat# ab256823 1:50
Anti-human Pan-CK Biolegend Cat# 914204; RRID: AB_2616960 1:800
Anti-human aSMA Biolegend Cat# 904601; RRID: AB_2565041 1:400
Anti-human LYVE-1 NOVUS Cat# NB110-61026 1:100
Antibodies for flow cytometry

Anti-mouse CD16/CD32 BioLegend Cat# 101302; RRID: AB_312801 0.5ug/test
BV510 Anti-mouse CD45 BioLegend Cat# 103138; RRID: AB_2563061 0.5ug/test
AF700 Anti-mouse CD3 BioLegend Cat# 100216; RRID: AB_493697 0.5ug/test
BV605 Anti-mouse CD8a BioLegend Cat# 100744; RRID: AB_2562609 0.5ug/test
BV50 Anti-mouse IFN-γ BioLegend Cat# 505832; RRID: AB_2734492 0.5ug/test
APC Anti-mouse Ki67 BioLegend Cat# 652406; RRID:AB_2561930 0.5ug/test
PerCP Anti-mouse CD11b BioLegend Cat# 101230; RRID:AB_2129374 0.5ug/test
AF488 Anti-CD11c BioLegend Cat# 117311; RRID:AB_389306 0.5ug/test
BV421 Anti-mouse CD31 BioLegend Cat# 102424; RRID:AB_2650892 0.5ug/test
PE Anti-mouse CD62P BioLegend Cat# 148306; RRID:AB_2565275 0.5ug/test
APC Anti-mouse CD326 BioLegend Cat# 118214; RRID:AB_1134102 0.5ug/test
PE/Cy7 Anti-mouse H-2Kb BioLegend Cat# 116520; RRID:AB_2721684 0.5ug/test
Fixable Viability Kit BioLegend Cat# 423105 1:1000
Antibodies for animal experiments
InVivoPlus anti-mouse PD-1 (CD279) BioXcell Cat# BE0146; RRID: AB_10949053 10mg/kg
InVivoPlus rat IgG2a isotype control BioXcell Cat# BP0089; RRID: AB_1107769 10mg/kg
Antibodies for Immunofuorescence staining
anti-human PD-L1 Abcam Cat# ab237726 1:800
anti-human CD15 Abcam Cat# ab135377 1:50
anti-human MPO Abcam Cat# ab208670 1:500
anti-human neutrophil elastase Cell Signaling Technology Cat# 90120 1:200

Validation

Antibodies for imaging mass cytometry:
HLA I (Abcam, Cat# ab239788) https://www.abcam.com/en-us/products/primary-antibodies/hla-class-1-abc-antibody-epr22172-bsa-and-azide-free-ab239788
CD14 (Abcam, Cat# ab226121) https://www.abcam.com/en-us/products/primary-antibodies/cd14-antibody-epr3653-bsa-and-azide-free-ab226121
FBLN5 (Abcam, Cat# ab66339) https://www.abcam.com/en-us/products/primary-antibodies/fibulin-5-antibody-1g6a4-ab66339
CD4 (Abcam, Cat# ab181724) https://www.abcam.com/en-us/products/primary-antibodies/cd4-antibody-epr6855-bsa-and-azide-free-ab181724
CD8a (Biolegend, Cat# 372902) https://www.biolegend.com/en-us/products/purified-anti-human-cd8a-antibody-13983
Collagen I (Abcam, Cat# ab215969) https://www.abcam.com/en-us/products/primary-antibodies/collagen-i-antibody-epr7785-bsa-and-azide-free-ab215969
TIGIT (Abcam, Cat# ab243903) https://www.abcam.com/en-us/products/primary-antibodies/tigit-antibody-blr047f-bsa-free-ab243903
IDO-1 (Proteintech, Cat# 66528-1-Ig) https://www.ptglab.com/products/IDO1-Antibody-66528-1-Ig.htm
LAG-3 (Abcam, Cat# ab241407) https://www.abcam.com/en-us/products/primary-antibodies/lag-3-antibody-sp346-bsa-and-azide-free-ab241407
CD68 (Biolegend, Cat# 916104) https://www.biolegend.com/en-us/products/purified-anti-cd68-antibody-13199
CD11b (Abcam, Cat# ab209970) https://www.abcam.com/en-us/products/primary-antibodies/cd11b-antibody-epr1344-bsa-and-azide-free-ab209970
CD20 (Abcam, Cat# ab213033) https://www.abcam.com/en-us/products/primary-antibodies/cd20-antibody-igel-773-bsa-and-azide-free-ab213033
PD-1 (CST, Cat# 63815SF) https://www.cellsignal.com/products/primary-antibodies/pd-1-intracellular-domain-d4w2j-xp-rabbit-mab-bsa-and-azide-free/63815
Ki-67 (BD, Cat# 550609) https://www.bdbiosciences.com/zh-cn/products/reagents/flow-cytometry-reagents/research-reagents/single-color-antibodies-ruo/purified-mouse-anti-ki-67.550609?tab=product_details
CD1C (Abcam, Cat# ab270797) https://www.abcam.com/en-us/products/primary-antibodies/cd1c-antibody-epr23189-196-bsa-and-azide-free-ab270797
HLA-DR (NOVUS, Cat# NB600-989) https://www.novusbio.com/products/hla-dr-antibody-tal-1b5_nb600-989
VEGFR2 (Abcam, Cat# ab315239) https://www.abcam.com/en-us/products/primary-antibodies/vegf-receptor-2-antibody-epr28328-80-bsa-and-azide-free-ab315239
CD57 (BD, Cat# 555618) https://www.bdbiosciences.com/zh-cn/products/reagents/flow-cytometry-reagents/research-reagents/single-color-antibodies-ruo/purified-mouse-anti-human-cd57.555618?tab=product_details
SELP (Abcam, Cat# ab54427) https://www.abcam.com/en-us/products/primary-antibodies/cd62p-antibody-pselko27-ab54427
Pan-CK (Biolegend, Cat# 914204) https://www.biolegend.com/en-us/products/purified-anti-pan-cytokeratin-antibody-13345
LYVE-1 (NOVUS, Cat# NB110-61026) https://www.novusbio.com/products/lyve-1-antibody-rm0033-4d17_nb110-61026
Antibodies for flow cytometry:
Fixable Viability Kit (BioLegend, Cat# 423105) https://www.biolegend.com/en-us/products/zombie-nir-fixable-viability-kit-8657
CD45 BV510 (BioLegend, Cat# 103138) https://www.biolegend.com/en-us/products/brilliant-violet-510-anti-mouse-cd45-antibody-7995
CD3 AF700 (BioLegend, Cat# 100216) https://www.biolegend.com/en-us/products/alexa-fluor-700-anti-mouse-cd3-antibody-3375
CD8a BV605 (BioLegend, Cat# 100744) https://www.biolegend.com/en-us/products/brilliant-violet-605-anti-mouse-cd8a-antibody-7636
IFN-γ BV650 (BioLegend, Cat# 505832) https://www.biolegend.com/ja-jp/products/brilliant-violet-650-anti-mouse-ifn-gamma-antibody-7681
Ki67 APC (BioLegend, Cat# 652406) https://www.biolegend.com/en-us/products/apc-anti-mouse-ki-67-antibody-8447
CD11b PerCP (BioLegend, Cat# 101230) https://www.biolegend.com/en-us/products/percp-anti-mouse-human-cd11b-antibody-4315
CD11c AF488 (BioLegend, Cat# 117311) https://www.biolegend.com/en-us/products/alexa-fluor-488-anti-mouse-cd11c-antibody-2702
CD31 BV421 (BioLegend, Cat# 102424) https://www.biolegend.com/en-us/products/brilliant-violet-421-anti-mouse-cd31-antibody-8599
CD62P PE (BioLegend, Cat# 148306) https://www.biolegend.com/en-us/products/pe-anti-mouse-rat-cd62p-p-selectin-antibody-10806

CD326 APC (BioLegend, Cat# 118214) https://www.biolegend.com/en-us/products/apc-anti-mouse-cd326-ep-cam-antibody-4974
H-2Kb PE/Cy7 (BioLegend, Cat# 116520) https://www.biolegend.com/en-us/products/pe-cyanine7-anti-mouse-h-2kb-antibody-15167
Antibodies for Immunofuorescence staining:
PD-L1 (Abcam , Cat# ab237726) https://www.abcam.com/en-us/products/primary-antibodies/pd-l1-antibody-cal10-ab237726
CD15 (Abcam, Cat# ab135377) https://www.abcam.com/en-us/products/primary-antibodies/cd15-antibody-sp159-ab135377
MPO (Abcam, Cat# ab208670) https://www.abcam.com/en-us/products/primary-antibodies/myeloperoxidase-antibody-epr20257-ab208670
neutrophil elastase (Cell Signaling Technology, Cat# 90120S) https://www.cellsignal.com/products/primary-antibodies/neutrophil-elastase-e8u3x-rabbit-mab/90120

Eukaryotic cell lines

Policy information about cell lines and Sex and Gender in Research

Cell line source(s)	For the construction of KRAS/p53 murine ICC models, plasmids were injected into mice by the hydrodynamic tail-vein injection at a 10:1 ratio of transposon to SB-luc transposase-encoding plasmid (25 μg of pT3-EF1a-KRASG12D plasmid) as well as 25 μg of the PX330-CRISPR/Cas9 sgRNA-p53 plasmid with the solution into the tail vein with a total volume corresponding to 10% of the body weight in 6 to 8 seconds. Vectors for hydrodynamic delivery were produced using the Qiagen Plasmid Plus Mega Kit. Equivalent DNA concentration between different batches of DNA was confirmed to ensure reproducibility among experiments. Mice were sacrificed 4-5 weeks after injection. The KPT cell line was derived from the KRAS/p53 murine ICC model in vitro, which was kindly gifted by Professor Qiang Gao from Zhongshan hospital, Fudan University, Shanghai.
Authentication	The cell line was authenticated by short tandem repeat (STR) profiling.
Mycoplasma contamination	The cell line was routinely tested for mycoplasma and tested negative throughout the course of these studies.
Commonly misidentified lines (See ICLAC register)	No commonly misidentified cell lines were used.

Palaeontology and Archaeology

Specimen provenance	*Provide provenance information for specimens and describe permits that were obtained for the work (including the name of the issuing authority, the date of issue, and any identifying information). Permits should encompass collection and, where applicable, export.*
Specimen deposition	*Indicate where the specimens have been deposited to permit free access by other researchers.*
Dating methods	*If new dates are provided, describe how they were obtained (e.g. collection, storage, sample pretreatment and measurement), where they were obtained (i.e. lab name), the calibration program and the protocol for quality assurance OR state that no new dates are provided.*

☐ Tick this box to confirm that the raw and calibrated dates are available in the paper or in Supplementary Information.

Ethics oversight	*Identify the organization(s) that approved or provided guidance on the study protocol, OR state that no ethical approval or guidance was required and explain why not.*

Note that full information on the approval of the study protocol must also be provided in the manuscript.

Animals and other research organisms

Policy information about studies involving animals; ARRIVE guidelines recommended for reporting animal research, and Sex and Gender in Research

Laboratory animals	C57BL/6 mice (female, 6–8 weeks of age)
Wild animals	This study did not involve wild animals.
Reporting on sex	Only female mice were included in this study due to animal housing requirements. Sex was not matter in the study design, since this study centers around cancer signaling and drug targets that generally do not require sex-based consideration.
Field-collected samples	This study did not involve samples collected from the field.
Ethics oversight	All animal breeding and experiments were conducted in accordance with institutional guidelines and were approved by the Institutional Animal Care and Use Committee guidelines (IACUC-2024-Mi-090). Animals were removed from the study and sacrificed if any signs of pain and distress were detected or if the tumor volume reached 2,000mm3. The maximal tumor size was not exceeded in all reported studies.

Note that full information on the approval of the study protocol must also be provided in the manuscript.

Clinical data

Policy information about clinical studies

All manuscripts should comply with the ICMJE guidelines for publication of clinical research and a completed CONSORT checklist must be included with all submissions.

Clinical trial registration	The ClinicalTrials.gov identifier is NCT05010668, preregistered at August 11, 2021.
Study protocol	The study protocol has been provided in the Supplementary Information.
Data collection	The efficacy of the treatment was evaluated in targeted lesion(s) using CT or MRI at baseline and at 6-week intervals following the initial administration of lenvatinib-sintilimab. Tumor responses determined using RECIST v1.1 criteria were specified by investigators in the study protocol and reported with an exact 95% confidence interval (CI). CR or PR was considered to be confirmed only if the criteria for each were met at a subsequent time point (4–6 weeks later). All adverse events (AEs) and serious AEs occurring within 30 days of the last dose were reported in accordance with the NCI Common Terminology Criteria for Adverse Events v5.0. The safety population was defined as all patients who received at least one dose of sintilimab, lenvatinib or cryoablation. Site-matched liver tumor biopsies from the same cryoablation-untreated lesion were obtained at three time points: baseline biopsy (pre-treatment), 2 weeks after cryoablation (post-cryoablation), and after the first two doses of lenvatinib and sintilimab (lenva+sint). Tumor lesions were punctured by 16-gauge needles twice or thrice at each sampling time. Tissue samples were kept in MACS Tissue Storage Solution (Miltenyi Biotec) and were processed for single-cell sequencing within 2 hours. PBMC samples were prepared using Lymphoprep solution (Stemcell Technologies) and were stored in liquid nitrogen and thawed for processing.
Outcomes	The primary end point was the investigator-assessed objective response rate (ORR), which was based on RECIST v1.1. The cryoablation-treated lesion was not included in the treatment response and was designated as a non-target lesion. The secondary end points were safety, investigator-assessed disease control rate (DCR), duration of response (DOR), progression free survival (PFS), and overall survival (OS). ORR was defined in accordance with RECIST v1.1 as the proportion of patients who achieved a confirmed best overall response of complete response (CR) or partial response (PR). DCR was defined as the proportion of patients who achieved CR, PR, or stable disease (SD). DOR was defined as the time from the first recorded CR or PR to disease progression or death for patients with CR or PR. PFS was defined as the time from enrollment to the first recorded imaging of disease progression or death from any cause, whichever occurred first. OS was defined as the time from enrollment to recorded death from any cause. Time to response (TTR) was observed as an exploratory end point in patients with post hoc response, defined as the time from enrollment to the first recorded, investigator-assessed CR or PR for confirmed patients. We also conducted exploratory analyses to examine the potential association of treatment response with a variety of immunologic parameters.

Dual use research of concern

Policy information about dual use research of concern

Hazards

Could the accidental, deliberate or reckless misuse of agents or technologies generated in the work, or the application of information presented in the manuscript, pose a threat to:

No	Yes	
☒	☐	Public health
☒	☐	National security
☒	☐	Crops and/or livestock
☒	☐	Ecosystems
☒	☐	Any other significant area

Experiments of concern

Does the work involve any of these experiments of concern:

No	Yes	
☒	☐	Demonstrate how to render a vaccine ineffective
☒	☐	Confer resistance to therapeutically useful antibiotics or antiviral agents
☒	☐	Enhance the virulence of a pathogen or render a nonpathogen virulent
☒	☐	Increase transmissibility of a pathogen
☒	☐	Alter the host range of a pathogen
☒	☐	Enable evasion of diagnostic/detection modalities
☒	☐	Enable the weaponization of a biological agent or toxin
☒	☐	Any other potentially harmful combination of experiments and agents

Plants

Seed stocks: n/a

Novel plant genotypes: n/a

Authentication: n/a

ChIP-seq

Data deposition

☐ Confirm that both raw and final processed data have been deposited in a public database such as GEO.

☐ Confirm that you have deposited or provided access to graph files (e.g. BED files) for the called peaks.

Data access links
May remain private before publication.

For "Initial submission" or "Revised version" documents, provide reviewer access links. For your "Final submission" document, provide a link to the deposited data.

Files in database submission

Provide a list of all files available in the database submission.

Genome browser session
(e.g. UCSC)

Provide a link to an anonymized genome browser session for "Initial submission" and "Revised version" documents only, to enable peer review. Write "no longer applicable" for "Final submission" documents.

Methodology

Replicates

Describe the experimental replicates, specifying number, type and replicate agreement.

Sequencing depth

Describe the sequencing depth for each experiment, providing the total number of reads, uniquely mapped reads, length of reads and whether they were paired- or single-end.

Antibodies

Describe the antibodies used for the ChIP-seq experiments; as applicable, provide supplier name, catalog number, clone name, and lot number.

Peak calling parameters

Specify the command line program and parameters used for read mapping and peak calling, including the ChIP, control and index files used.

Data quality

Describe the methods used to ensure data quality in full detail, including how many peaks are at FDR 5% and above 5-fold enrichment.

Software

Describe the software used to collect and analyze the ChIP-seq data. For custom code that has been deposited into a community repository, provide accession details.

Flow Cytometry

Plots

Confirm that:

☒ The axis labels state the marker and fluorochrome used (e.g. CD4-FITC).

☒ The axis scales are clearly visible. Include numbers along axes only for bottom left plot of group (a 'group' is an analysis of identical markers).

☒ All plots are contour plots with outliers or pseudocolor plots.

☒ A numerical value for number of cells or percentage (with statistics) is provided.

Methodology

Sample preparation

For flow cytometry, ectopic ICC tumor tissues were collected and processed into single-cell suspensions.Cells were first incubated with an anti-mouse CD16/CD32 antibody (BioLegend, Cat#101302) to block Fc receptors, followed by staining with specific antibodies on ice for 30 minutes.

Instrument

BD LSRFortessa X-20 flow cytometer (BD Pharmingen).

Software	FlowJo software (v10.8.1)
Cell population abundance	The cellular population abundance was determined by flow cytometry analysis of sorted cells as described in Fig.7.
Gating strategy	See Supplementary Fig.1 for gating strategy details.

☒ Tick this box to confirm that a figure exemplifying the gating strategy is provided in the Supplementary Information.

Magnetic resonance imaging

Experimental design

Design type	*Indicate task or resting state; event-related or block design.*
Design specifications	*Specify the number of blocks, trials or experimental units per session and/or subject, and specify the length of each trial or block (if trials are blocked) and interval between trials.*
Behavioral performance measures	*State number and/or type of variables recorded (e.g. correct button press, response time) and what statistics were used to establish that the subjects were performing the task as expected (e.g. mean, range, and/or standard deviation across subjects).*

Acquisition

Imaging type(s)	*Specify: functional, structural, diffusion, perfusion.*
Field strength	*Specify in Tesla*
Sequence & imaging parameters	*Specify the pulse sequence type (gradient echo, spin echo, etc.), imaging type (EPI, spiral, etc.), field of view, matrix size, slice thickness, orientation and TE/TR/flip angle.*
Area of acquisition	*State whether a whole brain scan was used OR define the area of acquisition, describing how the region was determined.*

Diffusion MRI ☐ Used ☐ Not used

Preprocessing

Preprocessing software	*Provide detail on software version and revision number and on specific parameters (model/functions, brain extraction, segmentation, smoothing kernel size, etc.).*
Normalization	*If data were normalized/standardized, describe the approach(es): specify linear or non-linear and define image types used for transformation OR indicate that data were not normalized and explain rationale for lack of normalization.*
Normalization template	*Describe the template used for normalization/transformation, specifying subject space or group standardized space (e.g. original Talairach, MNI305, ICBM152) OR indicate that the data were not normalized.*
Noise and artifact removal	*Describe your procedure(s) for artifact and structured noise removal, specifying motion parameters, tissue signals and physiological signals (heart rate, respiration).*
Volume censoring	*Define your software and/or method and criteria for volume censoring, and state the extent of such censoring.*

Statistical modeling & inference

Model type and settings	*Specify type (mass univariate, multivariate, RSA, predictive, etc.) and describe essential details of the model at the first and second levels (e.g. fixed, random or mixed effects; drift or auto-correlation).*
Effect(s) tested	*Define precise effect in terms of the task or stimulus conditions instead of psychological concepts and indicate whether ANOVA or factorial designs were used.*

Specify type of analysis: ☐ Whole brain ☐ ROI-based ☐ Both

Statistic type for inference (See Eklund et al. 2016)	*Specify voxel-wise or cluster-wise and report all relevant parameters for cluster-wise methods.*
Correction	*Describe the type of correction and how it is obtained for multiple comparisons (e.g. FWE, FDR, permutation or Monte Carlo).*

Models & analysis

n/a	Involved in the study
☐	☐ Functional and/or effective connectivity
☐	☐ Graph analysis
☐	☐ Multivariate modeling or predictive analysis

Functional and/or effective connectivity

Report the measures of dependence used and the model details (e.g. Pearson correlation, partial correlation, mutual information).

Graph analysis

Report the dependent variable and connectivity measure, specifying weighted graph or binarized graph, subject- or group-level, and the global and/or node summaries used (e.g. clustering coefficient, efficiency, etc.).

Multivariate modeling and predictive analysis

Specify independent variables, features extraction and dimension reduction, model, training and evaluation metrics.